DEVELOPMENT OF AN ACTIVE MAGNETIC REGENERATIVE REFRIGERATION SYSTEM FOR SUB-KELVIN COOLING OF SPACE INSTRUMENTATION

by

Chloe M. Gunderson

A thesis submitted in partial fulfillment of
the requirements for the degree of

Master of Science

(Mechanical Engineering)

at the

UNIVERSITY OF WISCONSIN – MADISON

2020

Approved:

DocuSigned by:
Franklin Miller
7A19E6BD7C5C462...

Professor Franklin K. Miller
Department of Mechanical Engineering
University of Wisconsin – Madison

DocuSigned by:
Greg Nellis
F92F784446FB475...

Professor Greg F. Nellis
Department of Mechanical Engineering
University of Wisconsin – Madison

Development of an Active Magnetic Regenerative Refrigeration System for Sub-Kelvin Cooling of Space Instrumentation

Research completed under the supervision of
Professors Franklin K. Miller and Greg F. Nellis at the University of Wisconsin – Madison

Abstract

Multiple state-of-the-art space science instruments used in far-IR, millimeter, and X-ray astrophysics missions require cryogenic operating temperatures for operation. Current refrigeration solutions for these detectors are far from ideal. ^{3}He evaporation refrigerators and Adiabatic Demagnetization Refrigerators (ADR)s, for example, are both presently used to reach cryogenic temperatures but require substantial amounts of magnetic shielding to protect the detectors, greatly increasing the weight of the system. Additionally, heat switches introduce additional inefficiencies, locations for possible failure, and weight into the system. Enhanced reliability and efficiency of detector cooling systems is vital to the success of future missions. The development of a sub-Kelvin Active Magnetic Regenerative Refrigerator (AMRR) addresses many of the challenges faced with current solutions as it can provide continuous and distributed cooling. The circulation of a ^{3}He-^{4}He mixture via a non-moving Superfluid Magnetic Pump (SMP) facilitates no-vibration cooling of multiple lower stages or detectors and makes cooling multiple locations on or within a detector possible. The need for heat switches is eliminated, and the amount of magnetic shielding is reduced because the instrument can be located at a further distance from the magnets.

The SMP used within the AMRR system was experimentally verified prior to this work, therefore this research focuses on the modeling and construction of the remainder of the system. Two regenerator canisters, two regenerator magnets, the cold heat exchanger (CHX),

and assembly support pieces are designed and machined to complete the system. The resulting proof-of-concept AMRR is designed to provide approximately 1 mW of cooling at 900 mK, and is a lightweight, efficient, non-vibrating cryogenic refrigeration solution. These qualities directly address the weaknesses in current solutions that are detailed in NASA's Science Instruments, Observatories, and Sensor Systems technology area (TA8) sub-goal 8.1.6.

Acknowledgments

There are many people to credit for their role in supporting my research efforts, and I am so thankful to have had so many positive mentors throughout my Master's program.

I would like to thank Amir Jahromi for his endless support and guidance in the past two years. He has always been more than willing to provide any information or advice he has, and my experience would have been very different without his generosity and expertise. I am fortunate to call him a mentor and friend.

I thank Jim Tuttle for his incredible mentorship as well, working with him was an incredible experience which taught me not only many lab skills but also how to think critically about problems in a way that I hadn't before. His encouragement played a large role in considering and eventually deciding to continue for my PhD, so I thank him for this as well.

I want to thank the entire NASA Goddard cryogenics branch, which is a group of exceedingly smart and kind individuals. They went out of their way to make me feel included and supported in the group, and through them I learned about the many considerations that go into developing space technology.

I would also like to thank Warren Holmes from NASA JPL, with whom I had the opportunity to work on a modeling project that required me to research an area of physics I was relatively unfamiliar with. Through this work, I gained a more thorough understanding of my own research and gained confidence in developing and exploring my own theories. Discussions with Warren helped me learn how to identify important behaviors to consider in cryogenic systems, and also taught me about a wide range of interesting topics related to our universe.

Thank you to the SEL group for always being willing to help when I have research or class questions, and for making the lab an inclusive, supportive, and enjoyable place to work. Also, thank you to Lucy Fitzgerald for all of her help in advancing this research. From machining to winding magnets to fixing the pump, she has had an impact in all of the major steps taken towards completing the assembly of the AMRR.

A big thank you to my close friends and family for giving me the confidence to pursue this fellowship and to take the next steps to pursue my PhD. Thank you for supporting me through my growing pains as I learned that unexpected outcomes are an important part of the research process and can be even more informative than achieving an expected outcome right away.

Finally, I would like to thank Prof. Franklin Miller and Prof. Greg Nellis for their advice and support. They are both excellent professors, and I have learned so much about thermodynamics and heat transfer through their classes. Thank you, Greg, for finding solutions to my research obstacles, whether it be your ability to easily identify new ways to approach a problem or find solutions that I didn't see myself, or your willingness to invest in whatever lab equipment or material is needed. This has allowed me to focus on advancing my research as much as possible in the time I have. Thank you, Franklin, for always being available to discuss and help with my research, my classes, and any other questions that I have. I have learned so

much through these discussions and you have challenged me to think creatively and at a higher level. Thank you also for teaching me to have more confidence in myself, without your encouragement I would not have applied for a Master's program or NASA fellowship and would not be in a position to continue for a PhD.

Funding

I would like to thank NASA for funding this research through a NASA Space Technology Research Fellowship, and for providing me with invaluable opportunities throughout the past two years through this fellowship.

Table of Contents

List of Figures

List of Tables

Nomenclature

B	Magnetic field strength (T)
$B_{axis,inside}$	Field along center axis of solenoid (T)
B_{eff}	Effective applied field (T)
b	Material background field (0.481 T for GGG)
C	Specific heat capacity (J/kg-K)
c	Specific heat capacity (J/mol-K)
E	Energy (J)
G(T)	Conductance (W/K)
g	Landé g-factor (2 for GGG)
g	Gibbs free energy
H	Applied magnetic field
h	Enthalpy (J/mol)
h^{os}	Osmotic enthalpy (J/mol)
I	Current (A)
J	Total electronic angular momentum (7/2 for GGG)
k_B	Boltzmann constant (1.38 x 10^{-23} J/K)
L_{coil}	Length of coil (m)
M	Number of temporal nodes
N	Number of spatial nodes
$\dot{N}$	Molar flow rate (mol/s)
NbTi	Niobium-Titanium
n	Number of atoms
n	Total turns per unit length (1/m)
p	Pressure
$\dot{Q}$	Heat transfer rate (W)
q_c	Critical heat flux (W/m^2)
R	Gas constant (8.314 J/mol-K)
R_{coil}	Effective coil radius (m)

S	Spin
S	Total entropy (J/K)
S_e	Conduction electron entropy (J/K)
S_l	Lattice entropy (J/K)
S_m	Magnetic entropy (J/K)
s	Specific entropy (J/mol-K)
T	Absolute temperature (K)
T_{ad}	Adiabatic Temperature (K)
T_b	Heat sink temperature (K)
T_C	Condensation temperature (K)
T_N	Neél Temperature (0.38 K for GGG)
U	Internal energy (J)
v	Molar volume
$\dot{W}$	Work transfer rate (W)
x	^{3}He molar concentration
x_2	Axial location of coil

Greek Symbols

I, II	Phase numbers
Δ	Change in value
κ_T	Isothermal Compressibility
λ	Lambda point (2.17 K)
μ	Chemical potential
μ_0	Permeability of free space ($4\pi \times 10^{-7}$ N/A^2)
μ_B	Bohr magneton (9.274×10^{-24} J/T)
Π	Osmotic pressure
ρ	Density (kg/m^3)

Superscripts

0	Pure substance

3	Helium-3
4	Helium-4

Subscripts

0	Initial state
1	Final state
3	Property of ^{3}He
4	Property of ^{4}He
CHX_in	Inlet to CHX
i	Spatial node index
j	Temporal node index
n	Normal state
max	Maximum value reached
s	Superfluid state

Acronyms

ADR	Adiabatic Demagnetization Refrigerator
AMRR	Active Magnetic Regenerative Refrigerator
CADR	Continuous Adiabatic Demagnetization Refrigerator
CHX	Cold heat exchanger
CV	Control Volume
DR	Dilution Refrigerator
FD	Flow Demagnetization
FM	Flow Magnetization
GEP	Galaxy Evolution Probe
GGG	Gadolinium Gallium Garnet
GLF	Gadolinium Lithium Flouride
HHX	Hot heat exchanger
ID	Internal Diameter
LHS	Left Hand Side

LNTP	Liters at Normal Temperature and Pressure
MW	Molar Weight
NFD	No Flow Demagnetization
NFM	No Flow Magnetization
OST	Origins Space Telescope
PICO	Probe of Inflation and Cosmic Origins
RHS	Right Hand Side
SEL	Solar Energy Lab
SMP	Superfluid Magnetic Pump
STJ	Superconducting Tunnel Junctions
TES	Transition Edge Sensor
TFN	Thermodynamic Fluctuation Noise
TX	Taxonomy Class

1 Introduction and Literature Review

1.1 Introduction

Cryogenic operating temperatures are vital to the success of numerous space science instruments used in far-IR, millimeter, and X-ray astrophysics missions. More specifically, missions from the ongoing Decadal Survey, expected to launch in 2035, require detector cooling at 50-100mK, with auxiliary cooling at or below 1K for various other devices such as telescope and optical components [1]. The Origins Space Telescope (OST), Probe of Inflation and Cosmic Origins (PICO), and Galaxy Evolution Probe (GEP) need detector cooling at 35-50 mK, 0.1 K, and 0.1 K, respectively, with 1 K auxiliary cooling [1]. Existing solutions are far from ideal, especially approaching sub-Kelvin temperatures, and significant advances in these refrigeration technologies would have widespread impact as many high sensitivity applications in current and future NASA missions rely on these cryogenic temperatures for operation.

^{3}He evaporation refrigerators and Adiabatic Demagnetization Refrigerators (ADRs) are presently used to provide sub-Kelvin cooling, but substantial amounts of magnetic shielding are needed to protect the instrument due to the proximity between the detector and magnets. This distance cannot easily be extended because of the requirement for a highly conductive thermal link between the system and the detector. Heat switches throughout the remainder of the system introduce additional inefficiencies, locations for possible failure, and weight into the system. Consequently, the system is much heavier than desired which is an important consideration for space technology. Additionally, scaling this system to increase cooling power would substantially increase the weight as the heavier components such as the shielding and

thermal links would need to scale similarly. These solutions also have necessary periodic recycling, which precludes continuous cooling and detector operation unless multiple units are used together and operated out of phase. This results in a higher required cooling power in precooling systems to shorten the recycle time requirements. Increased efficiency and reliability related to cooling these state-of-the-art low-noise detectors and optics would enable scientists to improve the resolution and range of data collection both in space and on the ground, allowing NASA to continue to push the bounds of human knowledge through discovery.

The development of a sub-Kelvin Active Magnetic Regenerative Refrigerator (AMRR) is discussed in this work. This novel AMRR addresses many of the challenges faced with current solutions as it can provide continuous and distributed Sub-Kelvin cooling via circulation of a ^{3}He-^{4}He mixture using a non-moving Superfluid Magnetic Pump (SMP). The resulting system is a no-vibration, low mass, and scalable Sub-Kelvin cooling solution for space instrumentation. Additionally, distributed cooling makes refrigeration of larger areas and within detectors possible, a significant advantage over other cryogenic refrigeration options.

1.2 Motivation for Mechanical Sub-Kelvin Cooling of Space Science Instrumentation

Cryogenic detectors have higher sensitivity and better energy resolution than alternative sensors, making them an attractive option for space exploration and essential for observing low energy photons in the near- or far-IR, X-ray, and submillimeter ranges [2]. Through low energy photon detection, NASA has been able to find terrestrial planets, examine cosmic background radiation, confirm the existence of interstellar dust, and map gravitational fields, among other things [2]. Since NASA's first cryogenic missions in the early 1980s,

increasingly complex space detectors have necessitated continuous advancements in cryogenic solutions [3]. Multiple current astrophysics photon detectors, such as Superconducting Tunnel Junctions (STJs), microcalorimeters, and Transition Edge Sensors (TESs), are dependent on mechanical coolers to achieve reliable and long-term cooling at the near Kelvin or sub-Kelvin operation temperatures; these are summarized in Table 1 [2]. Alternative refrigeration options fail to meet these requirements. Radiative cooling can only achieve cooling powers around 2 W at 50 K and stored-cryogen coolers can only reach near Kelvin temperatures with limited mission duration due to boil off [3].

Table 1. Characteristics of different photon detectors [2]. Near and sub-Kelvin detectors are highlighted.

Detector type:	Spectral range		Temperature range (K)		Dissipation range (W)		Detector size (pixel and array)	
	Range	Wavelength (m)	Min	Max	Min	Max	Pixel (μm)	Array (n x n)
Ge crystal	Gamma / hard X-ray	λ < 1E-11 m	50	100	0	0	10000	<10
CCD	X-ray / Vis	1E-10 < λ < 1E-6 m	150-200	300	0.1	20	10-30	10^6
STJs	X-ray–UV-Vis-NIR	1E-10 < λ < 5E-6 m	0.01	1	10^{-9}	10^{-6}	20-50	$<10^3$
μ-Calorimeters	X-ray	1E-10 < λ < 1E-7 m	0.05	0.3	10^{-12}	10^{-11}	100	<100
TESs	X-ray-UV-Vis-NIR	1E-10 < λ < 1E-6 m	0.05	0.3	10^{-11}	10^{-9}	100	<100
Photo-conductors-NIR	NIR	5E-7 < λ < 5E-6 m	30	100	0.01	0.02	30-50	10^6
Photo-conductors-MIR	MIR	5E-6 < λ < 5E-5 m	2	20	0.01	0.02	50-100	$<10^4$
Photo-conductors-FIR	FIR	5E-5 < λ < 1E-4 m	1	2	0.001	0.003	50-100	$<10^3$
Sub-mm bolometers	Sub-mm	1E-4 < λ < 1E-3 m	0.1	0.3	10^{-9}	10^{-8}	100-500	$<10^2$

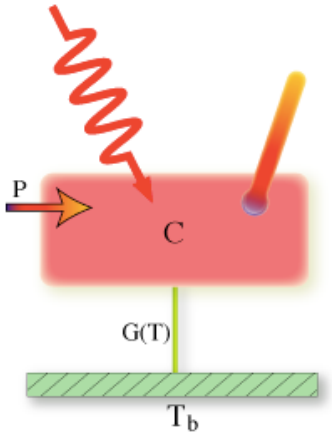

Figure 1. A visual depiction of a microcalorimeter [4].

These types of detectors rely on unique material properties existing only at cryogenic temperatures. For example, a microcalorimeter in its most elementary form consists of an absorber with C heat capacity, a thermometer, and a weak link to a cryogenically refrigerated heat sink at temperature T_b, as shown in Figure 1 [4]. The link has a conductance G, which is a function of its temperature. When an incident photon hits the absorber, the energy deposit causes the temperature of the absorber to spike,

which is detected by the thermometer and converted into an energy reading. The temperature then drops back to the baseline temperature as the heat is rejected through the thermal link to the heat sink. The change in temperature from an incident photon is inversely proportional to the heat capacity of the absorber, which quickly drops off as the temperature approaches 0 K. Thus cryogenic temperatures are required as lower-temperature absorbers have larger changes in temperature for a given photon and therefore are able to detect low energy levels with high resolution.

Similar to and sometimes in combination with microcalorimeters, TESs are thermometers that rely on cryogenic refrigeration, as they operate at the transition temperature of the superconducting films which comprise them [4]. These films are tuned to transition at the desired detector operating temperature, amplifying the change in resistance for small changes in temperature, as shown in Figure 2 [4]. Higher resistance changes for a given temperature change due to an incident photon increases the resolution of the energy reading even further.

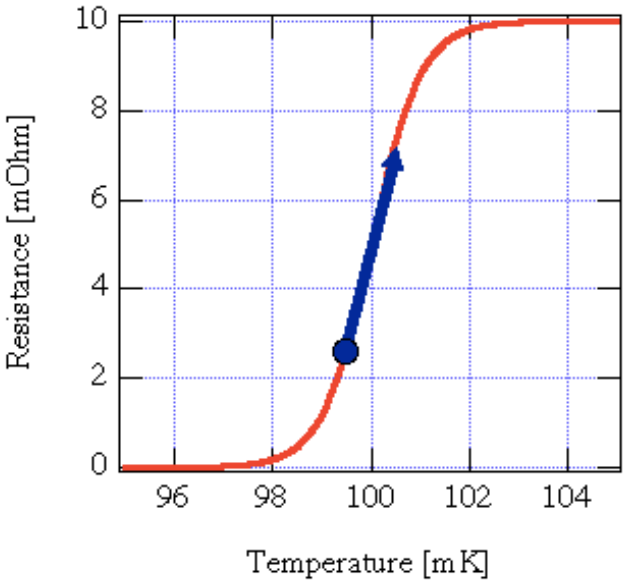

Figure 2. TES resistance as a function of temperature [4].

Perhaps more compelling, though, is the reduction of noise at cryogenic temperatures, which allows for more accurate measurements and smaller resolvable energy levels. The major sources of noise include thermodynamic fluctuation noise (TFN), thermometer Johnson or Nyquist noise, load resistor Johnson noise, amplifier noise, and photon background noise [5].

TFN appears in microcalorimeters and bolometers as energy exchanges between the absorber and the heat sink, resulting in energy fluctuations in the absorber [5]. The total error associated with this type of noise is proportional to the temperature. Likewise, thermometer and load resistor Johnson noises are temperature dependent and capture the thermal noise associated with thermal agitation of electrons within the thermometry circuit. These major thermal noise sources can be limited through cryogenic refrigeration. It is possible to reduce the remaining sources of noise to negligible levels through careful engineering of the amplifiers and optical components [5]. Figure 3 shows the effects of removing thermal sources of noise from a microcalorimeter, with c) showing the signal, TFN, and Johnson noise, b) removing the Johnson noise, and a) removing TFN [5].

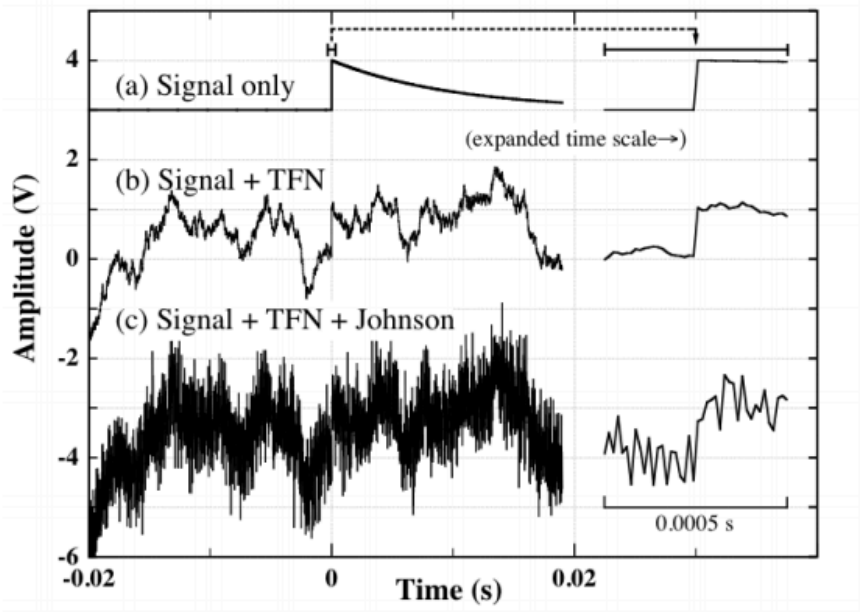

Figure 3. The signal from an ideal microcalorimeter with different types of noise [5].

It is clear that eliminating thermal noise sources increases the signal to noise ratio, ultimately enabling the detection of finer energy differences between photons and enhancing the resolution of the detector, as demonstrated in Figure 4. This graph is based on the

theoretical energy resolution of a microcalorimeter, which is given as $\Delta E \cong 2.35\sqrt{4kTE_{max}}$ where k is Boltzmann's constant, T is temperature, and E_{max} is the maximum incident photon energy [4]. For an incident photon with 10 keV of energy, lowering the operating temperature from 2 K to 0.5 K halves the minimum resolvable energy.

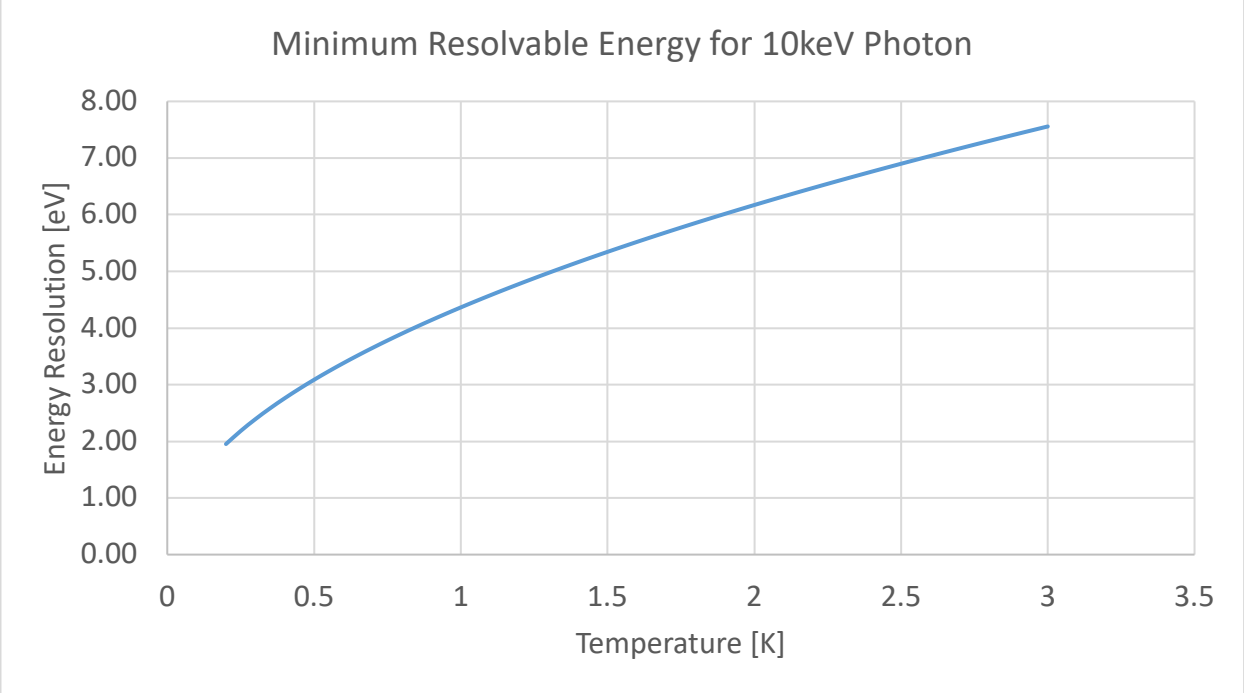

Figure 4. Theoretical minimum energy resolution in a microcalorimeter as a function of temperature for an incident photon with 10keV of energy.

1.3 Cryogenic Refrigeration Requirements for Current and Future NASA Missions

Numerous current and future NASA astrophysics missions have needs for cryogenic refrigeration as they are based on observations that are made possible with these low energy space instruments. LiteBird, ATHENA, and SPICA are all current or near-future missions which require sub-Kelvin cooling of their detectors [1]. Among SPICA's several instruments, SAFARI and BLISS both require sub-Kelvin cooling as they use TES bolometers for far-IR spectroscopy [6]. Chains of cryogenic systems must be creatively coupled to minimize mass

and provide the required cooling power at each instrument's operating temperature [6]. Efforts to advance cryogenic refrigeration systems will have a widespread impact on these missions as improved solutions could allow for increased efficiency, reduced mass, and, in some cases, continuous data collection. These capabilities will expand NASA's current limits for exploration and discovery, creating new possibilities for future missions. As previously noted, the upcoming Decadal Survey (scheduled to launch in 2035), which includes multiple detectors requiring millikelvin cooling with near Kelvin auxiliary cooling, could directly benefit from current research efforts.

It is evident that cryogenic refrigeration does and will continue to play a critical role in many NASA astrophysics missions. Therefore, to inform the direction of future research NASA has created guidelines outlining the requirements for advancements in this area. Two separate Taxonomies (TXs) in NASA's 2020 technology taxonomy discuss cryogenic solutions: Sensors and Instruments (TX08) and Thermal Management Systems (TX14).

Within the Sensors and Instruments category is the Cryogenic/Thermal subcategory (TX08.1.6). This category encompasses cryogenic systems with both passive and active components used to cool space instrumentation, the requirements being that they have "low power, low mass, and low exported vibration during operation" [7]. Adiabatic Demagnetization Refrigerators (ADRs), heat pipes, and cryocoolers are all example technologies in this category [7].

Under Thermal Management Systems is Thermal Conditioning for Sensors, Instruments, and High Efficiency Electric Motors (TX14.1.3), which includes "cost-effective, high-efficiency, low-weight/vibration cryocoolers and advanced sub-Kelvin cooling technology" [7]. These cryogenic solutions include technologies like magnetic refrigeration,

solid cryogens heat sinks, and liquid hydrogen spacecraft Dewars [7]. From this taxonomy, we can deduce that high efficiency and low mass, vibrations, and power are stringent requirements for future space instrument refrigeration solutions.

1.4 Current Near Kelvin and Sub-Kelvin Refrigeration Solutions

Sub-K coolers represent the coldest stage of cryogenic refrigeration chains, where the integration of numerous cooling solutions results in a wide-ranging system able to lift heat from the instrument to highest temperature heat sink (e.g. deep space). A variety of cryogenic space cooling systems, which are either presently used or under development, are shown in Figure 5, with their cooling powers given at typical operating temperatures.

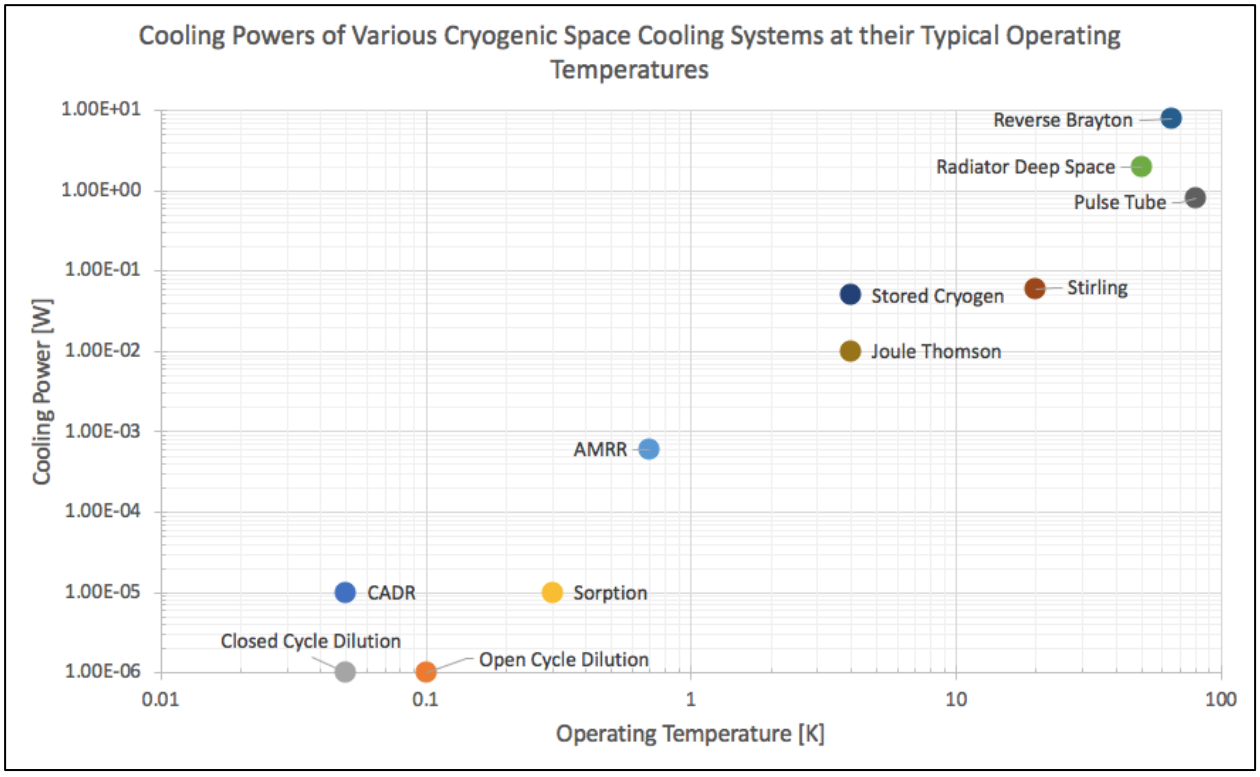

Figure 5. Cooling powers for cryogenic refrigeration solutions at a typical operating temperature. Data taken from [3] [32].

Early IR missions, such as IRAS, COBE, ISO, and Spitzer, relied solely on ^{4}He cryostats to achieve cryogenic operating temperatures between 1.4-3 K during flight [3]. It wasn't until the development of the ADR that the first sub-Kelvin mission, ASTRO-E, became possible. ASTRO-E was unfortunately lost during launch in 2005, but was designed to operate at 65 mK [3]. Subsequent development of new technologies has made achieving sub-Kelvin temperatures through different types of coolers feasible. In addition to the ADR, sorption coolers and open cycle dilution refrigerators have been used to reach these ultra-low operating temperatures in space. The focus of this research is on the development of a novel sub-Kelvin system, which addresses some of the challenges faced by these other solutions. In order to better understand the unique advantages of the AMRR system, it is important to provide a brief overview of the existing and near-future sub-Kelvin technologies for context.

1.4.1 Continuous Adiabatic Demagnetization Refrigerator (CADR)

Continuous Adiabatic Demagnetization Refrigerators (CADRs) are unique in that they can provide high power, long-term cooling at operating temperatures on the order of tens of millikelvin [3]. CADRs conform to many of NASA's requirements for space coolers, offering highly efficient, nonvibrational, and continuous cooling [8]. Figure 6 shows a diagram of the CADR, with the instrument on the left and the heat sink on the right [8].

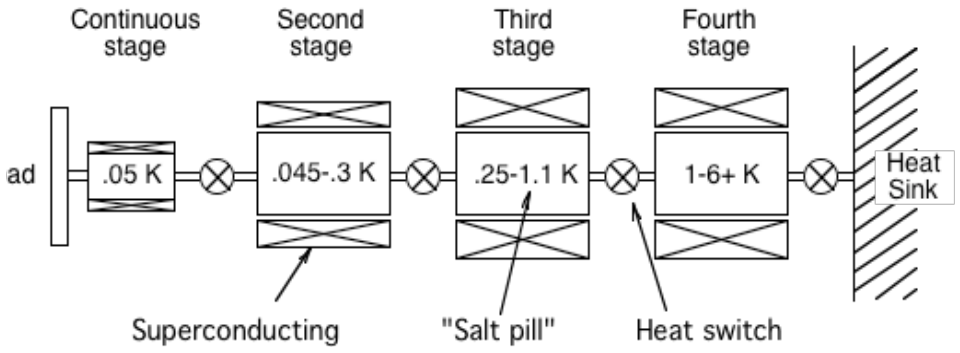

Figure 6. A diagram of the CADR system [8].

Each stage is composed of a salt pill surrounded by a superconducting magnet and magnetic shielding. The salt pills contain a paramagnetic refrigerant, therefore the temperature of the pill is linked to the applied magnetic field due to the magnetocaloric effect. Cycling through magnetizing and demagnetizing each stage, the system can lift heat from the instrument to the heat sink, allowing heat to move between stages via passive and active heat switches. This system is capable of maintaining a constant operating temperature for the instrument, and can provide 5-10μW of cooling at 50 mK [9] [8].

One of the disadvantages of this system is the large magnetic fields that are required. The requirement for a highly conductive thermal link between the system and detector limits the allowable distance between the two, placing the instrument in close proximity to the magnetic fields and necessitating substantial amounts of magnetic shielding, which adds significant mass. The heat switches are also an additional source of not only mass, but inefficiency and possible locations for failure within the system.

It should be noted that previous missions using this technology have actually used single-shot ADRs, which consist of just one of the previously described stages between the instrument and the heat sink. Though a single stage does not have as much weight as the complete CADR, it is not as robust an option because it cannot span as large of a temperature range or reach as low of temperatures, it has lower cooling power, and it cannot allow for continuous detector operation due to necessary periodic recycling of the single stage [8]. Due to these factors, NASA has been working to develop space-flight CADRs for future missions [8].

1.4.2 Dilution Cooler

Dilution refrigerators (DRs) are also presently used for refrigeration of space instrumentation. An open-cycle adaptation of a ground DR was developed for the Planck mission, and provided 0.1μW of continuous cooling at 0.1 K [10]. In this DR, gaseous ^{3}He and ^{4}He flowed from their respective reservoirs and were condensed into a mixing chamber where an endothermic mixing process dropped the temperature of the fluid and provided cooling at the cold tip. The resulting mixture was then pumped into space, limiting the cooler lifetime. For the Planck mission, 2.5 years of cooling was required, equating to 10,560 Liters at Normal Temperature and Pressure (LNTP) of ^{3}He and 31,680 LNTP of ^{4}He [10]. In upcoming missions, especially those with longer lifetimes, the open-cycle DR is impractical as the amount of required cryogens becomes too great.

Efforts are underway to create a gravity-insensitive closed-cycle DR, which would have a longer lifetime, reach temperatures in the tens of millikelvin, and offer cooling powers that are closer to the very high cooling powers (on the order of 100 μW at 0.1 K) that are normally associated with ground DRs [3] [10]. Though further development of this technology will address many of the weaknesses in the current DR solution, this is not a fully demonstrated option at this time.

1.4.3 ^{3}He/^{4}He Sorption Pump Cooler

^{3}He/^{4}He sorption pump coolers are also an option for sub-Kelvin space refrigeration. These closed-cycle coolers are simple in operation, requiring no moving parts and offering high efficiency duty cycles [3]. FIR instruments on the *Herschel* Space Observatory relied on a ^{3}He sorption cooler to reach operating temperatures of 285 mK for large arrays of

bolometers [11]. An exploded representation of the space-flight system is shown in Figure 7 [11].

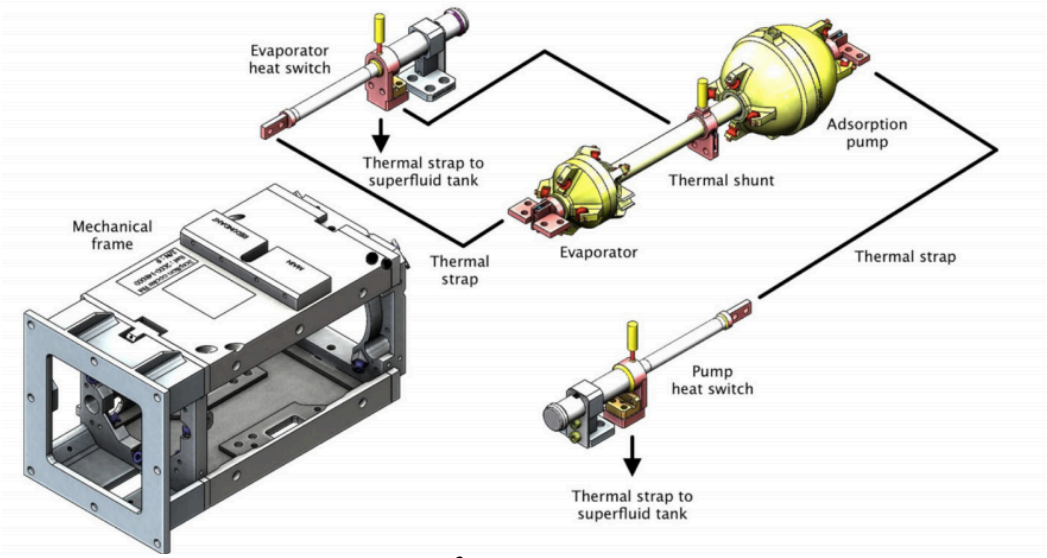

Figure 7. An exploded view of the ^{3}He sorption cooler used on *Herschel* [11].

In this system, liquid ^{3}He is trapped within a porous alumina sponge in the evaporator and provides cooling to the detector as it evaporates [11]. Activated charcoal in the sorption pump is used to drive this evaporation through adsorption, effectively pumping on the helium vapor and lowering the saturated vapor pressure and temperature [12]. The relationship between saturated vapor pressure and temperature for ^{3}He and ^{4}He is shown in Figure 8 [12].

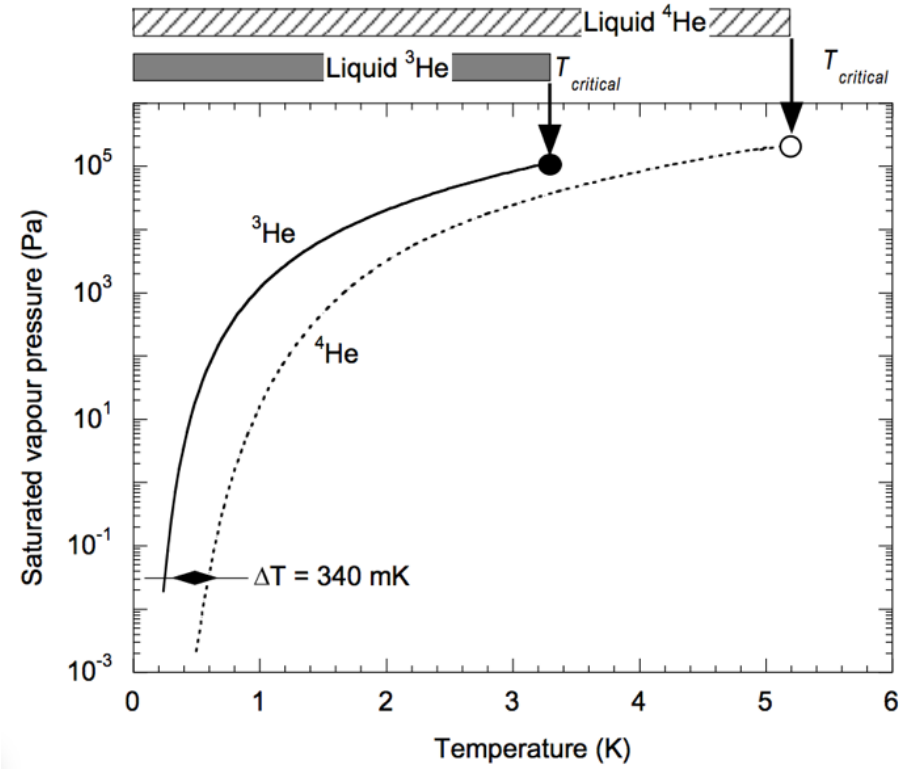

Figure 8. Saturated vapor pressure of helium 3 and helium 4 [12].

Physical adsorption occurs when a gas particle collides with a surface at a low enough temperature that the incident particle loses a substantial amount of kinetic energy and remains attached to the surface through weak intermolecular forces [13]. Porous materials maximize sorption capacity due to their large surface areas (typically 1200 m^{2}/g for activated charcoal) [12] [13]. The adsorption process continues until all of the helium is gaseous [11]. At this point, the recycling procedure begins. The recycling procedure is controlled by heaters and gas-gap heat switches throughout the system [11]. The sorption pump is heated to desorb the trapped helium gas, eventually outgassing and condensing the helium back on the evaporator which is thermally linked via a heat switch to a liquid ^{4}He bath at around 1.7 K [11]. To finish the procedure, the heat switch to the evaporator is opened, and the heat switch between the pump and the liquid bath is closed [11]. Cooling the charcoal causes it to begin pumping again,

lowering the ^{3}He pressure and dropping the temperature of the liquid ^{3}He to the 300 mK operating temperature [11]. The *Herschel* system could provide a hold time between 60 and 73 hours, with recycling times of 2-3 hours [11].

Though the duty cycle in this system is long, the periodic operation necessarily prevents continuous cooling. Additionally, similar to the ADR, the reliance on heat switches and heaters results in inefficiency in the system as these components produce substantial waste heat – for the 10 μW detector load on *Herschel*, the total heat rejected to the liquid bath was 23 mW [9]. The adsorption of helium also limits the system. To maintain low pressure during pumping, the helium layer on the charcoal surfaces should not exceed a few monolayers of gas; beyond this point the adsorption effect becomes negligible and the helium pressure and temperature will increase [13]. An additional consequence of the reliance on adsorption is that the operating temperature is limited to about 300 mK for ^{3}He and 1 K for ^{4}He - temperatures corresponding to the achievable saturated vapor pressure in the system using a sorption pump. The adsorption process also necessitates desorbing the gas from the charcoal getter each cycle, requiring heating to tens of Kelvin and contributing to the previously mentioned waste heat [9].

1.4.4 Comparison of Current Solutions and the AMRR

Though there are only a small number of systems able to reach near and sub-Kelvin temperatures, there are enough difference between these solutions in categories of importance to require careful consideration when designing for specific missions. In many cases it may be suitable to chain even these sub-Kelvin coolers in series, using systems with higher base temperatures such as the AMRR or sorption cooler as precooling systems for lower temperature systems to take advantage of each coolers' unique strengths. Table 2 synthesizes

and condenses these system descriptions, drawing attention to some of the most important considerations for each system: cooling power, base temperature, and key advantages and disadvantages. To allow for comparison, the AMRR that is the subject of this work has been added to Table 2.

Table 2. A comparison of current space refrigeration systems and the AMRR, adapted from [9].

Space Cooler	Power at Base Temperature	Advantages	Disadvantages
CADR	5-10μW at 50 mK	Long lifetime	Heat switches
		High cooling power	High magnetic fields
		Lowest base temperature	
Open-Cycle Dilution	1μW at 100 mK	Continuous	Eventual boil off
		Promising future developments	Low efficiency
			Must transport cryogen
^{3}He/^{4}He Sorption	10μW at 300 mK	Efficient duty cycle	Not continuous
		Closed-cycle	Reliance on heaters/heat switches
		Non moving	Low thermodynamic efficiency
AMRR	600μW-1mW at 900 mK	Distributed cooling	Not flight ready
		Scalable	Highest base temperature
		Long lifetime	

The AMRR system developed in this research will provide cooling down to approximately 900 mK with a predicted cooling power of 600μW-1mW, though future iterations with different types of magnetic refrigerant could reduce the cold end temperature. This system has no vibrations, is low mass, and has high efficiency and therefore has many of the characteristics laid out in the NASA guidelines. A specific advantage of this system is that the cooling is provided via circulation of a ^{3}He-^{4}He mixture, so instrumentation can be located

at a greater distance from the magnetic cooler than in existing systems. Lengthening this distance will reduce the magnetic shielding needed, therefore lowering the weight of the refrigeration system as a whole. The flow of the ^{3}He-^{4}He mixture will eliminate the need for the traditional copper heat bus that is otherwise required. The use of an active magnetic regenerator eliminates the need for the heat switches between stages in ADRs, further decreasing the weight of the overall system. The circulation of ^{3}He-^{4}He will also allow sub-K cooling to be distributed within instruments or over larger areas, allowing larger detectors and/or multiple detectors to be cooled with one magnetic cooler. Additionally, scaling this system to increase cooling power would not increase the weight substantially, unlike in other systems where the heavier components such as the shielding and thermal links would need scale similarly. A substantial improvement over current cryogenic systems, this technology will reduce the mass of the refrigeration unit while maintaining reliable cooling of sensitive instruments and therefore represents an important step forward in cryogenic refrigeration technology.

1.5 Introduction to the AMRR System

A superfluid magnetic pump (SMP), two regenerators, one cold heat exchanger, and two hot heat exchangers comprise the AMRR system shown in Figure 9 [9]. The left hand side (LHS) and right hand side (RHS) operate identically and 180° out of phase of each other. This is a novel AMRR in that it uses the nearly thermodynamically reversible SMP to displace the fluid, resulting in a system with no moving parts. This greatly increases the reliability of the system and makes it a strong candidate for use in space for cooling sensitive instruments.

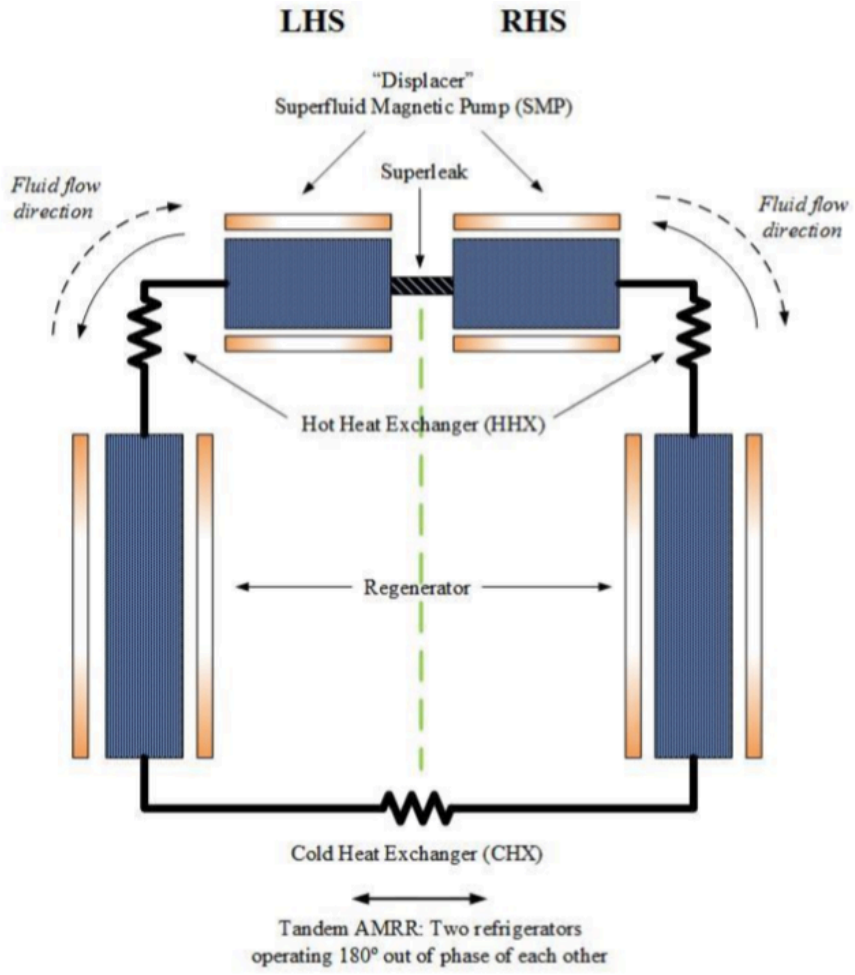

Figure 9. A diagram of the AMRR system developed at UW-Madison [9].

Shown in Figure 10, the SMP is composed of two separate canisters filled with finely crushed paramagnetic Gadolinium Gallium Garnet (GGG) particles that are suspended within the hollow bores of superconducting magnets. A superleak with 4 nm pores connects the two pump canisters and allows superfluid ^{4}He to move freely between the two beds. To produce flow, the current in one coil is increased while the coil in the opposite coil is decreased, resulting in increasing and decreasing magnetic fields, respectively. The shift in applied fields causes the thermal and magnetic entropies in the paramagnetic beds to also change due to the magnetocaloric effect. As the magnetic field in one canister rises, the magnetic entropy of the

GGG must decrease. The thermal entropy thus increases, offsetting the magnetic change to the total entropy and raising the overall temperature. Because the ^{3}He-^{4}He is in good thermal contact with the GGG, the fluid tracks the temperature of the particles very closely. The increase in temperature promotes a portion of the ^{4}He from the superfluid state to the normal state, and forces fluid to exit the canister through the normal port into the rest of the system. The opposite is true for the canister experiencing a decreasing magnetic field. The superleak maintains continuity in the system, allowing only superfluid ^{4}He to cross from the cooling canister into the warming canister to replace the promoted ^{4}He. Flow in the system is reversed by alternating between increasing and decreasing the magnetic fields in each canister.

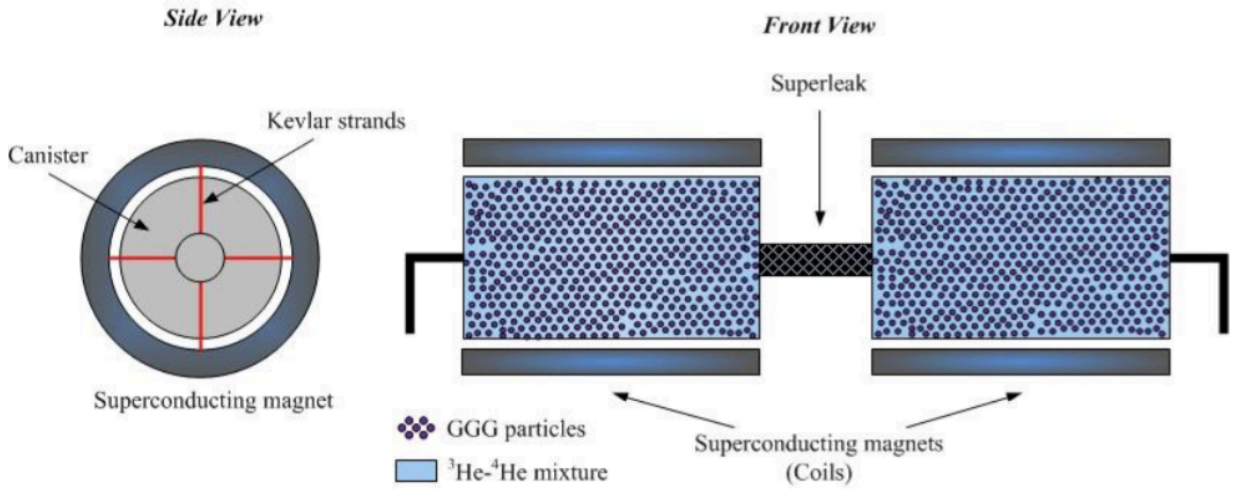

Figure 10. Visual representation of the Superfluid Magnetic Pump (SMP) [9].

The magnetic regenerators are almost identical in construction to the pump. Canisters of crushed paramagnetic GGG are suspended inside the bore of superconducting solenoids by Kevlar strands. As fluid is forced out through the warming pump bed, it moves down through the demagnetizing regenerator, which cools the mixture so that it exits the bed at the desired outlet temperature. The mixture then moves through a cold heat exchanger (CHX), providing

sub-Kelvin cooling to the load (e.g., one or more detectors). It flows back up through the opposite, magnetizing regenerator which rejects more heat into the fluid. Finally, this heat is rejected to the precooling stage at a temperature around 1.6 K. The system can then be reversed, sending flow back in the opposite direction. A more detailed full AMRR cycle explanation is provided in section 3.2.1. The circulatory nature of this system is one of the most important differences between the AMRR and other cryogenic refrigeration systems with similar applications as it addresses many of the aforementioned inefficiencies, making it an attractive option for future space science missions.

1.6 Research Objectives

The ultimate goal of this research is to design and construct a complete proof-of-concept AMRR system to show that it is a viable option for cryogenic cooling of space instrumentation. A simple numerical model of the system was created for use as a design tool to size the components required by the system. Many of the SMP components were already available so the bulk of the design/fabrication work was focused on the remaining AMRR components. The regenerator canisters were fabricated, packed with crushed GGG to the desired porosity, and sealed. Two superconducting magnets were wound for the regenerators, and a pre-existing but unused replacement magnet was installed into the SMP. A second SMP replacement magnet was also designed. The resulting AMRR system will use four new superconducting magnets, and will be assembled within the cryostat and filled with the ^{3}He-^{4}He mixture to allow experimental testing.

2 GGG and ^{3}He-^{4}He Background

2.1 Introduction

The AMRR technology relies on the manipulation of key physical characteristics of the refrigerant and fluid contained within the system. Specifically, the use of paramagnetic GGG links the temperature of the material to the applied magnetic field through the magnetocaloric effect, allowing for induced temperature change within the system as a response to changing magnetic fields. Similarly, ^{3}He-^{4}He mixtures have unique properties that result in temperature driven flow. A basic introduction to the foundational intricacies of the AMRR is critical to understanding the system as a whole.

2.2 Magneto-Caloric Effect and Applications

The magnetocaloric effect or adiabatic temperature change is the heating or cooling of the material due to the interaction between magnetic moments in the material and a changing external magnetic field [14] [15]. The magnetic moments are attributed to the unfilled electron shells in some ions in the refrigerant, resulting in a total electronic angular momentum (J) of each of these ions [15]. When these moments align with an external magnetic field, the magnetic entropy (S_m) within the material is reduced. The resulting effect on temperature can be better understood looking at the total entropy of a magnetic solid (S), which is a function of both the magnetic field strength (B) and absolute temperature (T):

$$S = S_m(B,T) + S_l(T) + S_e(T). \quad (1)$$

The magnetic entropy becomes much larger than the lattice entropy (S_l) and entropy of conduction electrons (S_e) at low temperature, so this is the main consideration for cryogenic applications [15]. The magnetic portion of the entropy can be represented by the following

equation, assuming that the magnetic moments within a material do not interact with each other:

$$\frac{S_m(T,B)}{R} = x \cdot \left(\coth(x) - (2J+1) \cdot \coth\left(x \cdot (2J+1)\right)\right) + \ln\left(\frac{\sinh\left(x \cdot (2J+1)\right)}{\sinh(x)}\right) \quad (2)$$

$$\text{where } x = \frac{\mu_B g B}{2 k_B T}. \quad (3)$$

where the parameters include the gas constant R (8.314 J mol^{-1} K^{-1}), the Bohr magneton μ_B (9.27·10^{-24} J/T), the Boltzmann constant k_B (1.38·10^{-23} J/K), the total electronic angular momentum J, and the Landé g-factor g [15]. The magnetic entropy also depends on the ratio of B/T; therefore, changing the applied magnetic field necessarily changes either the total entropy of the material or the temperature.

The link between temperature and applied magnetic field in a magnetic material is demonstrated visually in Figure 11 [14]. A material is initially at S_0, T_0, and applied magnetic field $H_0 = 0$. If the material is adiabatically and reversibly magnetized to H_1, the total material entropy remains constant; this process is represented by the horizontal arrow in Figure 11. The magnetic contribution to the entropy reduces as the magnetic ions align with the increased magnetic field. Consequently, the thermal entropy and temperature increase, maintaining constant total entropy in the system. This is captured in equations (2) and (3), where holding S_m constant while increasing B must increase T as well. Thus, the final state has a higher temperature due to the magnetization of the material. This process is reversible, and therefore with an adiabatic demagnetization the system can return to its initial state. The work done on the system is analogous to the adiabatic compression and expansion of a gas.

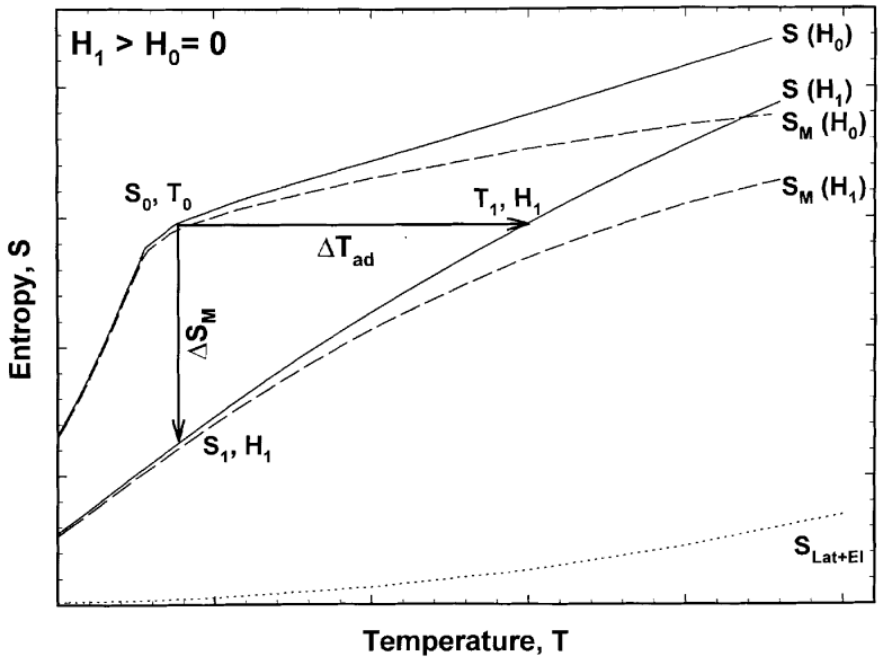

Figure 11. Visual representation of isothermal and adiabatic magnetization process in a magnetic material, indicated by vertical and horizontal arrows respectively [14].

At the opposite limit, a magnetic material undergoing an isothermal magnetization is also shown in Figure 11 by the vertical arrow. In this process, temperature and thermal entropy are constant by definition; therefore the magnetization reduces the total entropy of the system as the magnetic moments become coupled to the increasing field. Heat must be removed from the magnetic material in order to maintain a constant temperature.

This effect was originally discovered in iron by Warburg in the late 1800s, and later proposed to achieve ultra-low temperatures through adiabatic demagnetization by Debye and Giauque [9]. Using the magnetocaloric effect, temperatures below the boiling point of liquid helium were achievable – the lowest reachable temperature at that time [9].

2.2.1 Paramagnetic Material Properties

Though the magnetocaloric effect can be observed in all magnetic material, materials that are paramagnetic at low temperatures have been the focus of early sub-K cooling research. The magnetocaloric effect in paramagnets is maximized at temperatures approaching 0 K where the lattice heat capacity becomes negligible [14]. However, at a low enough temperature (which is material-dependent) known as the Néel or Curie temperature, most paramagnetic materials become magnetically ordered into ferro-/ferrimagnetic or antiferromagnetic states, severely reducing the zero field entropy and refrigerant efficacy [15] [16]. In selecting a paramagnetic salt for magnetic refrigeration, it is important to choose a material that is suitable for the temperature range of the system to ensure maximum adiabatic temperature change without risking material ordering. In this context, a variety of other factors should be considered as well, for example:

- larger magnetocaloric response is seen with large angular momentum J and Landé factor g;
- large thermal conductivity helps minimize temperature gradients;
- the material should exhibit small magnetic and thermal hysteresis;
- the material should be simple to make good thermal contact with;
- the material should be non-toxic, corrosion resistant, and easy to form; and
- the material should have a reasonable cost [15].

Table 3 contains various paramagnetic refrigerants that have sub-K ordering temperatures [15]. The temperatures listed in the table are the lowest temperatures achieved during heat capacity measurements of the materials, and are the same as the refrigerant ordering temperatures in most cases. However, it should be noted that more recent research

has reported that GLF has an ordering temperature below 0.25 K [16]. The system developed in this research is designed to provide cooling at a temperature no lower than 0.7 K, making Gadolinium Gallium Garnet (GGG) and Gadolinium Lithium Flouride (GLF) attractive options as they have ordering temperatures of 0.38 K and 0.25 K, respectively; temperatures closest to the design temperature without risk of ordering. These two options have identical angular momentums and Landé factors, and both are often used as refrigerants at higher sub-K and low Kelvin temperatures.

Table 3. Angular momentum, Landé factor, lowest temperature achieved in measurements, and magnetic ion density for various paramagnetic refrigerants [15].

Refrigerant	Chemical Composition	J [1]	g [1]	T_o [K]	N [cm^{-3}]
CMN	$Ce_2Mg_3 \cdot (NO_3)_{12} \cdot 24H_2O$	1/2	2	0.0015	$1.65 \cdot 10^{21}$
CCA	$CrCs(SO_4)_2 \cdot 12H_2O$	3/2	2	0.01	$2.09 \cdot 10^{21}$
CPA	$CrK(SO_4)_2 \cdot 12H_2O$	3/2	2	0.009	$2.21 \cdot 10^{21}$
FAA	$Fe(SO_4)_2NH_4 \cdot 12H_2O$	5/2	2	0.026	$2.14 \cdot 10^{21}$
MAS	$Mn(SO_4)_2(NH_4)_2 \cdot 6H_2O$	5/2	2	0.17	$2.79 \cdot 10^{21}$
DGG	$Dy_3Ga_5O_{12}$	15/2 [a]	8	400	$1.28 \cdot 10^{22}$
GGG	$Gd_3Ga_5O_{12}$	7/2	2	0.38	$1.26 \cdot 10^{22}$
GLF	$GdLiF_4$	7/2	2	0.48	$1.34 \cdot 10^{22}$

As shown in Table 3, GLF has a slightly higher ion density than GGG, translating to a 20 to 60 percent larger entropy change than that of GGG [15]. However, GGG is still a suitable and widely used refrigerant at this temperature, has high thermal and transport properties, has good chemical stability, is a reasonable cost, and is easily crushed to the desired particle size [9] [15]. For the proof-of-concept AMRR developed in this research, GGG was chosen as the refrigerant for both the SMP and the regenerators, partially due to the large amount of GGG available to the UW-Madison Solar Energy Lab (SEL). Future iterations could use multiple stages of different refrigerants to reach lower temperatures.

2.2.2 GGG as a Refrigerant

As previously noted, GGG is often used in higher temperature ranges, typically from approximately 1 K up to 20 K; although the magnetocaloric effect diminishes approaching the upper temperature limit [15]. The low end is somewhat limited by the Néel temperature, though the magnetic moments in GGG below this temperature interact in a way that does not lead to one preferred spin orientation and so magnetic ordering into an antiferromagnetic (AFM) state is dependent on the presence of an applied field as shown in Figure 12 [17] [15].

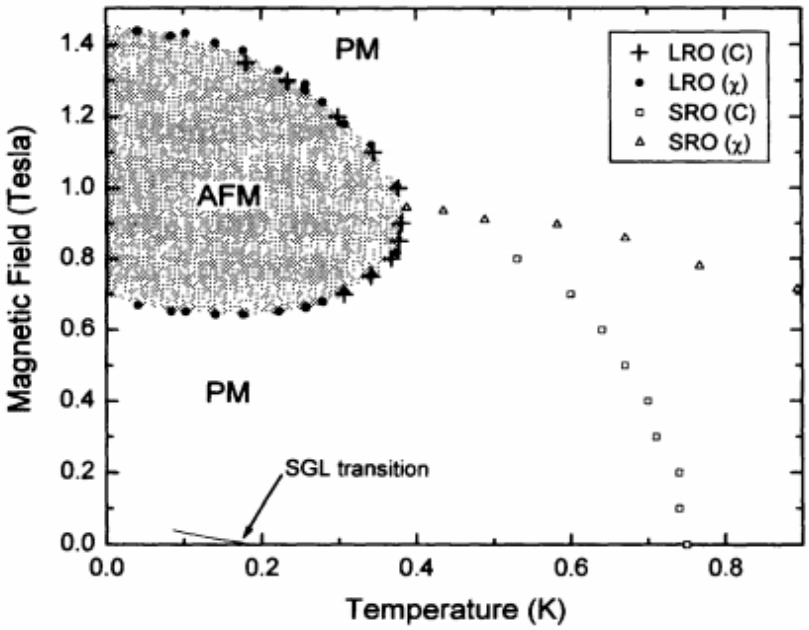

Figure 12. The magnetic phase diagram for GGG showing the paramagnetic (PM) and antiferromagnetic (AFM) states as functions of the temperature and applied field [17].

The AMRR system design temperature range is between 0.7 K and 1.8 K, well within the upper and lower bounds of GGG's useful temperature range. For this system, the entropy of the GGG can be modeled with a slight adaption of equations (2) and (3) in order to account for interaction between magnetic moments. These interactions should be accounted for with

an effective *B* value that averages the applied field with the material background field, *b,* which is 0.481 T for GGG [16]:

$$B_{eff} = \sqrt{B^2 + b^2}. \quad (4)$$

Using this correction, specific entropy for GGG is shown as a function of temperature for various applied fields in Figure 13. We can see that the zero field entropy for material at 700 mK is about 9 J/mol-K. If this material is adiabatically magnetized to *B* = 1 T, the temperature will increase from 700 mK to 1.6 K – an adiabatic temperature change ΔT_{ad} of close to 1 K.

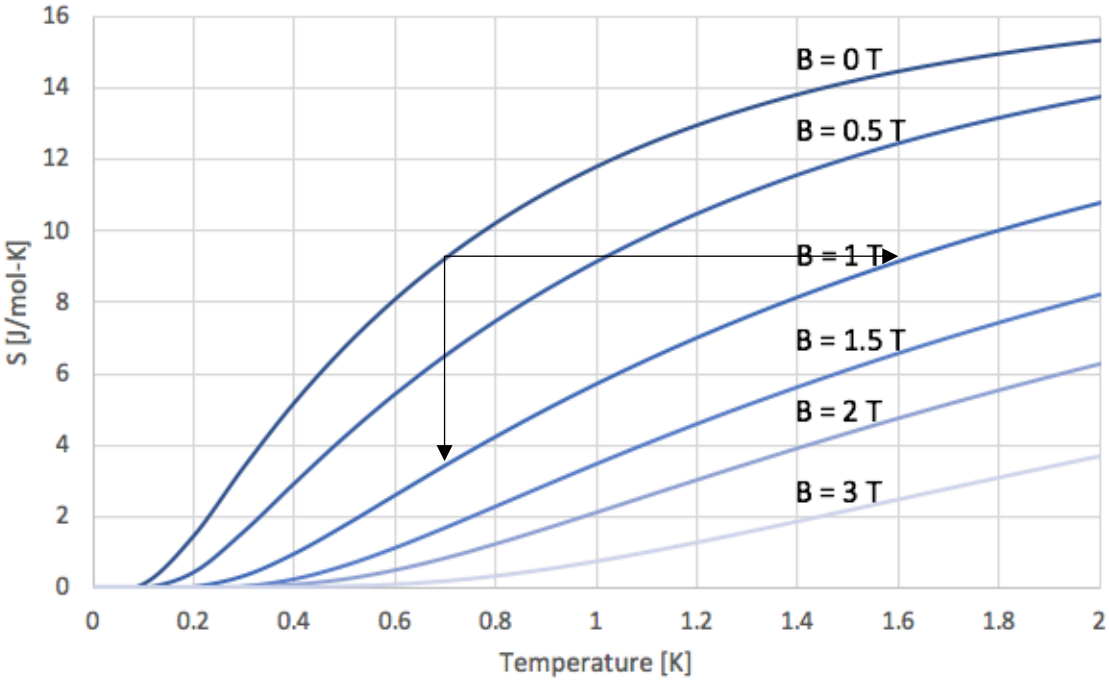

Figure 13. Specific entropy values for GGG as a function of temperature for select applied fields.

At the opposite limit, isothermal magnetization of GGG at 700 mK to *B* = 1 T will result in a final entropy of about 3.5 J/mol-K. With a total ΔS_M of 5.5 J/mol-K, 3.85 J/mol of heat must be rejected from the GGG. The regenerators within the AMRR system operate between these two limits.

The specific heat capacity of GGG can be found taking the derivative of the entropy with respect to temperature at constant field and multiplying by the temperature:

$$C(T,B) = R \cdot x^2\left(\frac{1}{\sinh^2(x)} - \frac{(2J+1)^2}{\sinh^2(x(2J+1))}\right). \quad (5)$$

The specific heat capacity for GGG is shown as a function of temperature for various applied magnetic fields in Figure 14.

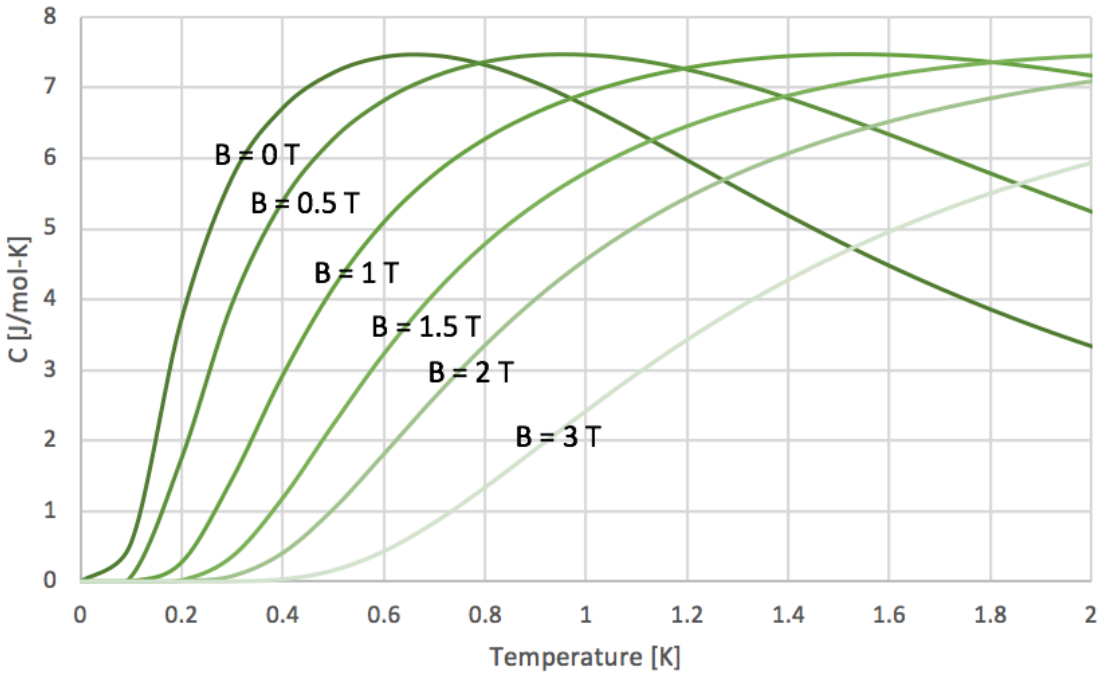

Figure 14. Specific heat capacity of GGG as a function of temperature for various magnetic fields.

A summary of important GGG properties, including molar weight (MW) and density (ρ), are provided in Table 4.

Table 4. Important GGG material properties.

Refrigerant	J [-]	g [-]	b [T]	T_N [K]	ρ [kg/m^3]	MW [kg/mol]
GGG	7/2	2	0.481	0.48	7080	1.012

2.3 Low Temperature Helium Properties

Helium is the only element that is liquid in the temperature range of operation for the AMRR, making it the sole option for the system working fluid. In fact, helium will only freeze at pressures more than 20 times atmospheric pressure, and has boiling points of 4.2 K for ^{4}He and 3.2 K for ^{3}He – both well above the maximum temperature seen within the cooler [18]. At low temperatures, each of the two stable helium isotopes exhibits unique properties. As a mixture, their respective properties, as well as interaction effects between the individual isotopes, contribute to the overall usefulness of the ^{3}He-^{4}He fluid in the AMRR system.

2.3.1 Pure ^{3}He

Of the two naturally occurring isotopes, ^{3}He is significantly less abundant than ^{4}He, representing only 1 ppm of total helium [19]. The quantities of ^{3}He needed for research purposes did not become available until after WWII when the nuclear weapons program began producing ^{3}He as a byproduct of nuclear reaction. This production exceeded demand until 2001, at which point the stockpile of ^{3}He began to decrease [20]. In recent years, a significant reduction in ^{3}He supply has driven up the price from $100-$200 per liter to over $2,000 per liter from commercial sources [21]. One proposed solution to this shortage is mining ^{3}He from lunar soil, which contains large amounts of the isotope from incident solar wind that is able to reach the moon's surface because there is no atmosphere [22]. Though the technology needed to do this requires further development, the motivation for securing a more abundant ^{3}He supply is convincing because of the widespread applications that rely on properties unique to ^{3}He, including MRI machines, nuclear and radiological material detection, and cryogenic cooling [20].

As previously mentioned, helium is unique in that it is the only element that does not solidify unless it is subjected to high pressures. This is due to both its strong zero point fluctuations and its weak intermolecular forces [19]. Zero point motion refers to the oscillations of quantum particles about their average position, and grows stronger in particles with small atomic mass like helium [19]. Having two protons but only one neutron, ^{3}He has a total nuclear spin of ½ and obeys Fermi-Dirac statistics, resulting in its unusual low temperature properties [19]. The Pauli exclusion principle states that only one particle can fill each available state in Fermi systems, and at absolute zero temperature the energy of the highest occupied state is known as the Fermi Energy E_F of the system [19]. This energy can be used to find the Fermi temperature, below which the gas is degenerate (i.e. all states are filled). For ^{3}He, this temperature is around 1 K [19].

At temperatures on the order of 1 mK and below, two different superfluid phases – where the ^{3}He atoms become frictionless – are observed [19]. The formation of these superfluid states is analogous to that of superconductive states in metals; the ^{3}He fermions form Cooper pairs which condense into the same quantum state, though in ^{3}He the spins align parallel with each other (S=1) [19]. In the presence of a magnetic field, a third stable phase emerges between A and the normal Fermi liquid, and the A phase becomes stable down to zero pressure [19]. However, this occurs significantly below the operating temperature of the AMRR and is out of the scope of this research. In the temperature range of the AMRR system, ^{3}He is a normal liquid as shown in the phase diagram in Figure 15 [19].

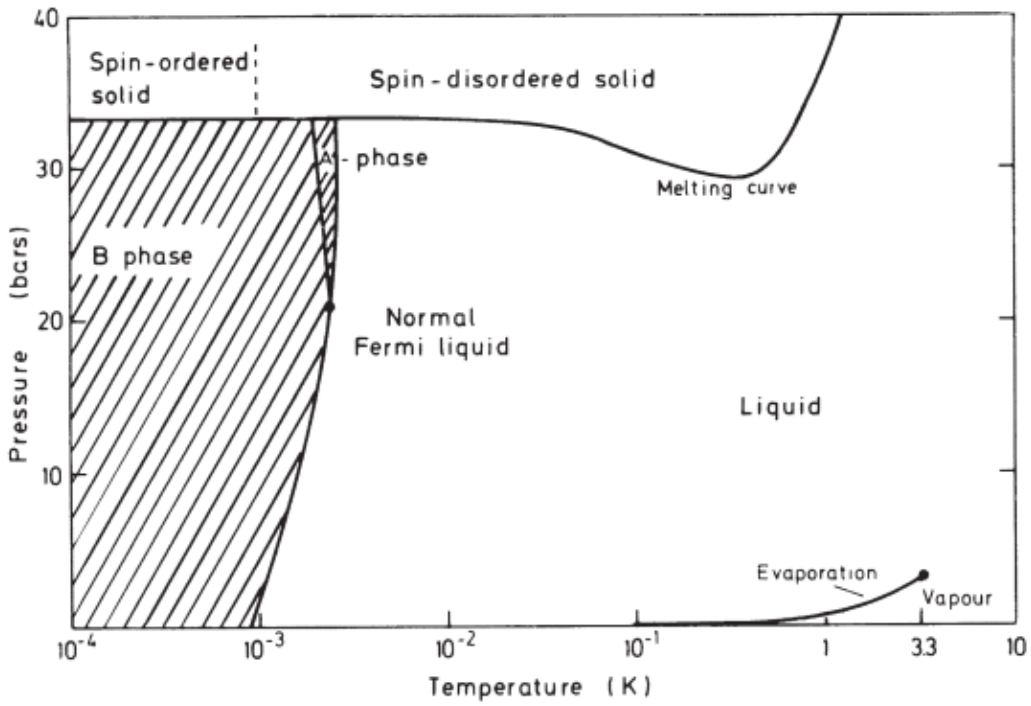

Figure 15. ^{3}He Phase diagram [19].

2.3.2 Pure ^{4}He

The more common isotope, ^{4}He, is the element traditionally referred to as "helium" and contains two protons and two neutrons [19]. It is the heavier of the two isotopes, and has a higher binding energy than ^{3}He, resulting in its higher boiling point [23]. Unlike ^{3}He, the ^{4}He atom has zero spin and obeys Bose-Einstein statistics [23]. Below the condensation temperature T_C, an increasing fraction of bosons occupies the lowest energy state, a phenomenon known as Bose-Einstein condensation [23]. In ^{4}He, this transition point is referred to as the λ-transition and occurs around 2.17 K, where normal liquid ^{4}He begins transitioning into a superfluid [23]. The ^{4}He phases at temperatures above and below this transition have markedly different properties and are commonly called He I and He II, respectively. These ^{4}He phases are shown in Figure 16 [19].

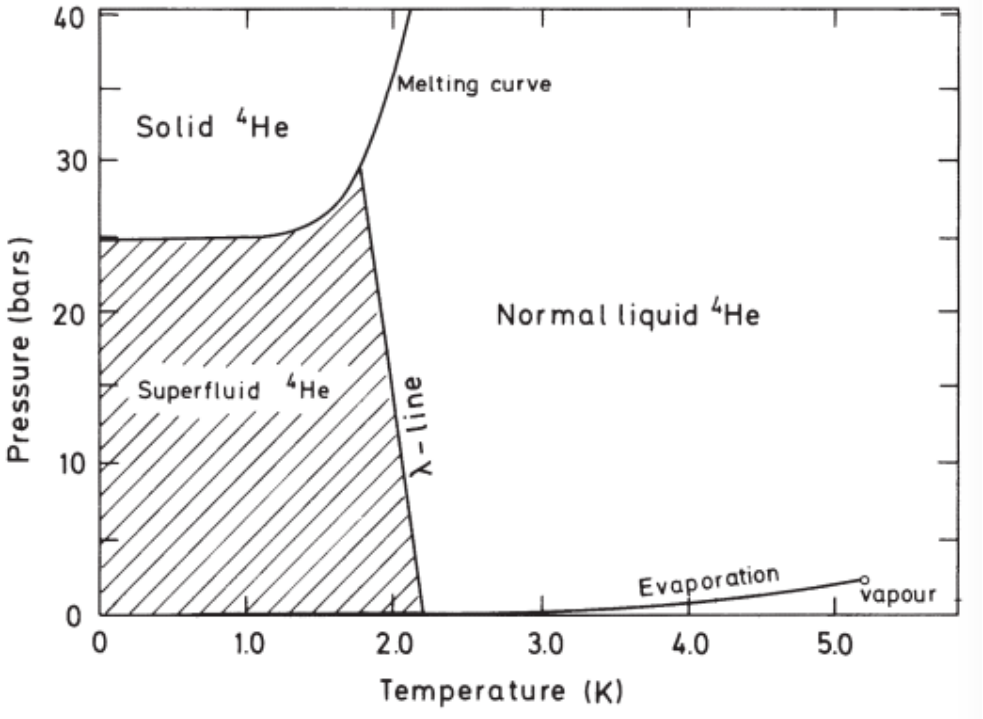

Figure 16. ^{4}He phase diagram [19].

He I and He II states never exist simultaneously, and the second-order phase transition between them makes clear their unique independent thermodynamic state properties. The He I and He II heat capacities are shown in Figure 17, separated by the discontinuity at the lambda temperature where the slope of the entropy is also discontinuous [23]. The normal fluid in the He I phase acts similarly to classical fluids, and is even comparable to a weakly interacting gas due to its low viscosity and intermolecular attraction [23]. He II, on the other hand, is a quantum fluid and exhibits truly remarkable properties that are beyond classical comparison. This phase can be explained using Tisza and Landau's two-fluid model which states that He II is composed of both normal fluid, which contains the excitations and behaves as an ordinary liquid, and superfluid, which has no viscosity and no entropy [23]. The relative portions of normal fluid and superfluid are temperature dependent, and the ratios of normal (ρ_n) and superfluid (ρ_s) densities to the bulk liquid density are shown in Figure 18 [23]. At 1 K, 99% of

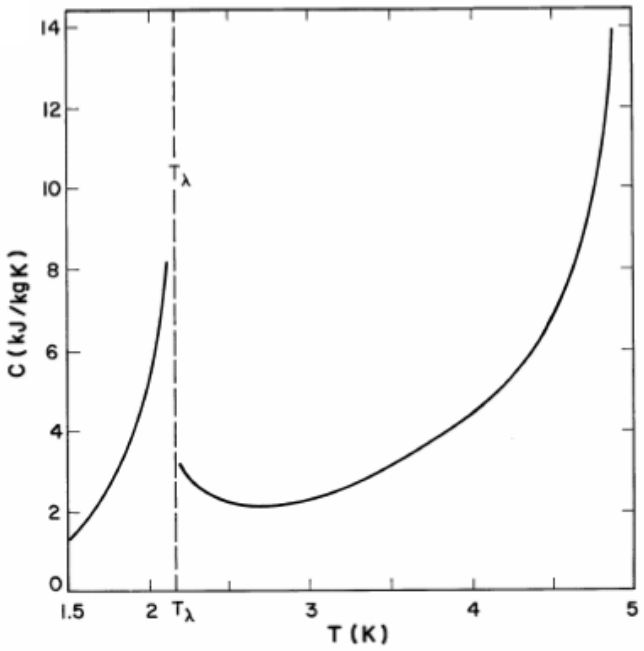

Figure 17. ^{4}He heat capacity as a function of temperature. He I and He II phases are shown on the right and left sides of the lambda temperature T_λ, respectively [23].

He II is in the superfluid state, which cannot carry heat, and is responsible for the rapid drop in heat capacity below the lambda temperature [23]. This is in contrast to ^{3}He, whose large magnetic spin entropy gives rise to a large heat capacity: 40 times larger than the heat capacity of ^{4}He at 1 K.

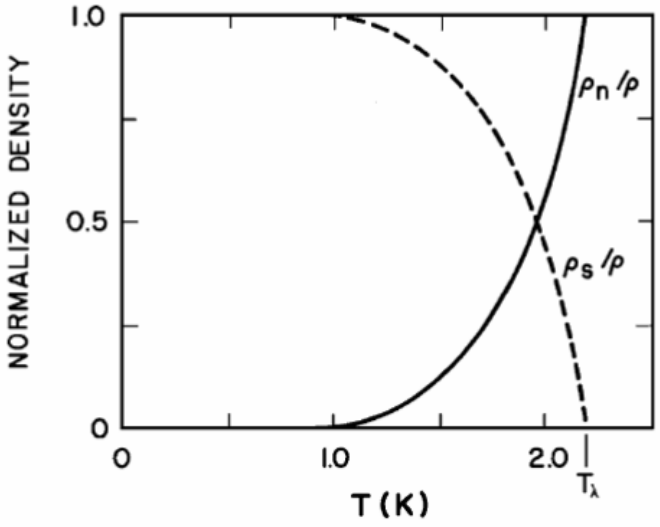

Figure 18. Superfluid and normal fluid density normalized to bulk He II density as a function of temperature [23].

He II exhibits somewhat unusual transport properties, which can be explained using the two-fluid model. For example, the viscosity of a fluid can be measured through two different methods that generally giving the same result. In the first method, measuring the laminar flow rate through a

capillary with a known pressure drop can be used to determine the viscosity. For ^{4}He, the viscosity calculated from this test becomes vanishingly small after entering the He II state [23]. However, the second method – rotating a disk emerged in the liquid and measuring damping – shows an increase in viscosity as the temperature is lowered beyond about 1.8 K. This unexpected difference can be explained considering both components of the fluid. In the first method, the normal fluid interacts with the capillary walls and is mostly locked in place. The superfluid can move without resistance through the channel and consequently comprises the measured flow, so the apparent viscosity is very small. With the second method, the normal fluid component must flow against its own viscous drag, and the resulting viscosity measurement is actually representative of the viscosity of the normal fluid portion.

Strange behavior is evident with respect to thermal transport in the liquid. In general, He II has a conductivity several orders of magnitude larger than highly conductive metals, reaching 100 kW/m-K in wide channels [9]. Interestingly, for He II subjected to an axial heat flux, the conductivity is a proportional function of tube diameter up to a critical heat flux, q_c [23]. The diameter dependence does have an upper limit, however, as increasing the diameter decreases the critical velocity [23]. If the diameter is too large and the fluid exceeds the critical velocity, the flow will become turbulent and significantly reduce conductivity because of impeded superfluid motion within the bulk fluid [23].

Below the critical heat flux a proportional relationship exists between the temperature gradient and pressure gradient. The thermomechanical fountain effect is evidence of this relationship. This effect is demonstrated by placing a vessel of He II in a bath of He II and using a porous superleak to allow only superfluid to exchange between the two bodies of fluid. A superleak is a plug with pores on the order of a nanometer through which superfluid can

flow without resistance, but normal fluid is blocked. The setup is shown in Figure 19 [23]. Both bodies are initially near 1 K, then a heater is used to raise the temperature of the inner vessel, promoting superfluid to the normal state, raising the pressure, and forcing normal liquid to fountain out of the top. The resulting pressure difference drives the flow of superfluid from the bath into the vessel through the superleak, replacing the exiting normal fluid. This superfluid flow can also be explained considering the He II chemical potential, which is maintained at the same value for both bodies through this exchange. The relationship between superfluid flow direction and temperature change can be determined given:

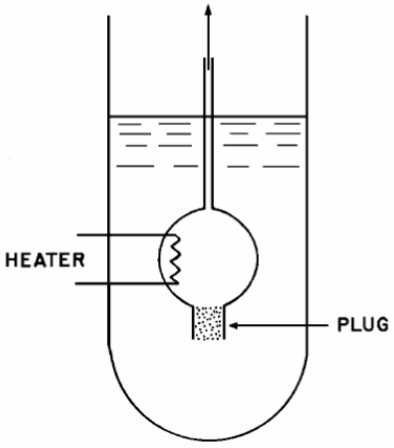

Figure 19. Experimental setup to demonstrate fountain effect in He II [23].

$$\left.\frac{\partial n}{\partial T}\right|_{\mu} = -n^2 \kappa_T \left.\frac{\partial \mu}{\partial T}\right|_{n} \tag{6}$$

where κ_T is a positive isothermal compressibility, n is the number of atoms in the body of fluid, T is the temperature, and μ is chemical potential [24]. For He II, $\partial\mu/\partial T|_n$ becomes negative around 1 K, meaning that increasing the temperature of the vessel reduces the chemical potential and results in an influx of superfluid atoms driven to find a new equilibrium potential between the two bodies [24].

2.3.3 ^{3}He-^{4}He Mixture Properties

Some cryogenic applications require a mixture of both isotopes, capitalizing on the unique individual properties of both ^{3}He and ^{4}He, and the way they interact as a mixture. Some of these properties can be observed from the ^{3}He-^{4}He mixture phase diagram shown in Figure

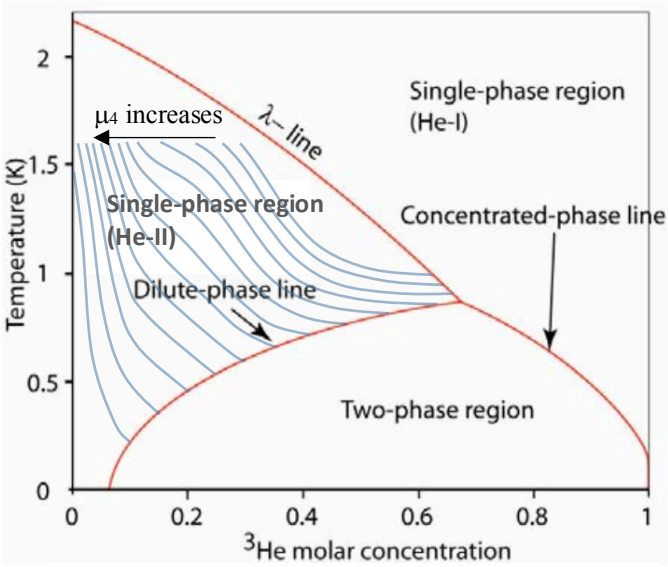

Figure 20. Phase diagram for ^{3}He-^{4}He mixtures at saturated pressure [25].

20 [25]. In order to specify the state of the mixture, three independent properties are needed [25]. The phase diagram shown is at saturated pressure, with temperature and ^{3}He molar concentration, x, as the two additional independent properties. In calculating mixture state properties, it is sometimes helpful to use ^{4}He chemical potential, μ_4, as one of the independent variables instead of x or T, so lines of constant μ_4 have been added to the diagram. As seen with ^{4}He, the lambda line separates regions of single-phase He I and He II in the mixture, though increasing the ^{3}He concentration depresses the temperature at which this transition occurs. The lambda line terminates at the tri-critical point, where T = 0.872 K and x = 66.9% ^{3}He [23]. At temperatures below this point, there exists a phase-separation region where the mixture separates into a dilute phase with He II and lower ^{3}He concentration, and a concentrated phase with He I and higher ^{3}He concentration [23]. This is the region of interest for dilution refrigeration, as very low temperature cooling in this system is provided by transferring ^{3}He from a pure phase into the dilute phase, a process with a finite entropy of mixing.

It is critical to stay within the single-phase He II region while operating the AMRR for a variety of reasons. The superfluid component of the He II is vital to the operation of the SMP, which relies on the fountain effect to circulate fluid throughout the system. One canister is warmed while the opposite is cooled, causing superfluid to rush from the cooling one into the

warming one to equalize chemical potential in the system and forcing normal fluid into the system. As can be observed by the lines of constant chemical potential in Figure 20, in a system of equal chemical potential the cold end has higher concentrations of ^{3}He. This results in a higher heat capacity in the cold heat exchanger than if He II were used alone. Recall that at temperatures below 1 K, ^{3}He has a heat capacity that exceeds 40 times the heat capacity of ^{4}He. To demonstrate this effect, the mixture heat capacity for various ^{3}He concentrations is shown in Figure 21 [25]. This experimental data has been smoothed, but effectively shows the impact of even small amounts of ^{3}He in increasing the overall mixture heat capacity.

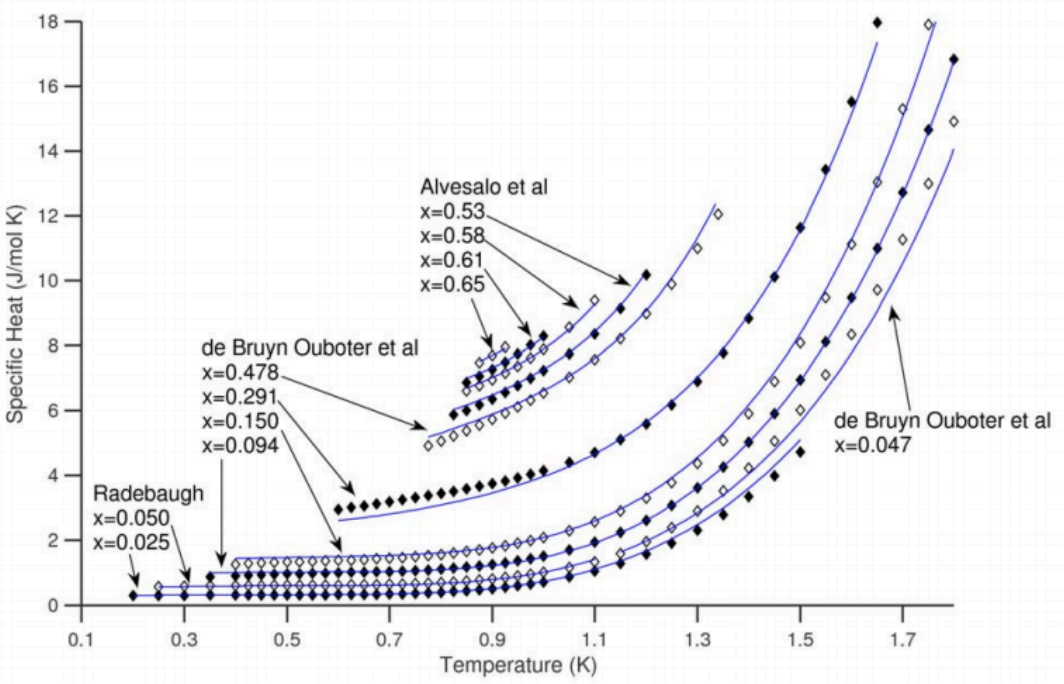

Figure 21. Specific heat of ^{3}He-^{4}He mixture for various concentrations [25], with data from [26] [27] [28].

Understanding the behavior of the mixture in the He II region is important for determining how to calculate some of the fluid properties used to model the system; specifically the osmotic pressure and enthalpy, which take special consideration of the superfluid behavior in the fluid. The osmotic pressure can be explained looking at the pressure

difference between two chambers connected by a superleak, one filled with the ^{3}He-^{4}He mixture and the other filled with pure ^{4}He. At equilibrium, the pressure in the ^{4}He chamber is lower than the other chamber by an amount known as the osmotic pressure [25]. Because of the superleak link, the superfluid is able to flow between chambers to maintain an equal chemical potential. This gives us the following relationship:

$$\mu_4(p, T, x) = \mu_4^0(p - \Pi, T), \tag{7}$$

where μ_4^0 is the chemical potential of the pure ^{4}He at the same temperature, T, as the mixture chamber but a pressure lower by the osmotic pressure, Π [25]. Taking a Taylor expansion and eliminating higher order terms, we find the osmotic pressure is defined by:

$$\Pi(p, T, x) = \frac{\mu_4^0(p, T) - \mu_4(p, T, x)}{v_4^0(p, T)} \tag{8}$$

where v_4^0 is the molar volume of pure ^{4}He [25]. As x increases at a constant temperature, μ_4 decreases, which can be observed looking at lines of constant chemical potential in Figure 20. Therefore according to Eq. 8, the osmotic pressure increases with increasing x and decreasing μ_4.

Perhaps more useful for modeling the AMRR system is an understanding of the osmotic enthalpy of the mixture, h^{os}, which was first introduced by London, Clarke, and Mendoza [29]. It is defined per mole of ^{3}He as:

$$h^{os} = \frac{h - (1 - x)\mu_4}{x} \tag{9}$$

where h is the enthalpy of the bulk flow of the mixture per mole. The use of osmotic enthalpy is an important adjustment made to the traditional First Law of Thermodynamics to account for the superfluid portion of the mixture, which moves at a different velocity than the bulk flow

of normal fluid which is viscously interlocked, and thus requires that enthalpy term to be separated into two values:

$$\frac{dE}{dt} = \dot{Q} - \dot{W} + \sum_{ports} \dot{N} h_{flow} = \dot{Q} - \dot{W} + \sum_{ports} \dot{N}_3 h^{os} + \sum_{ports} \dot{N}_4 \mu_4 \tag{10}$$

where E is the total energy in the control volume, $\dot{Q}$ is the rate of heat transferred to the control volume, $\dot{W}$ is the rate of work transferred out of the control volume, and $\dot{N}_3$ and $\dot{N}_4$ are the rates of molar flow into the control volume for ^{3}He and ^{4}He, respectively [25]. The derivation of this corrected energy balance comes from the energy balance of the Gedanken apparatus shown in Figure 22 [25] [30] [31]. A ^{3}He-^{4}He mixture enters the control volume from the port on the right with a total molar flow rate of $\dot{N}$, and flows freely into the top canister, which is at the same pressure, temperature, and concentration as the entering mixture. Superfluid from the entering mixture flows into the bottom canister via the superleak at a molar flow rate of $\dot{N}_{4s}$, flowing at a rate that equalizes the chemical potentials of the two canister. This pure ^{4}He canister is maintained at the mixture temperature through contact with a thermal reservoir, and has a pressure less than the other canister by the osmotic pressure. The resulting molar flow rate into the top canister is then $\dot{N}_3 + \dot{N}_4 - \dot{N}_{4s}$, reflecting the ^{3}He and ^{4}He molar flow rates into the system less the superfluid portion that entered the bottom canister. At steady state, this fluid displaces the existing fluid within the control volume in each canister at the same rate that it enters. For the

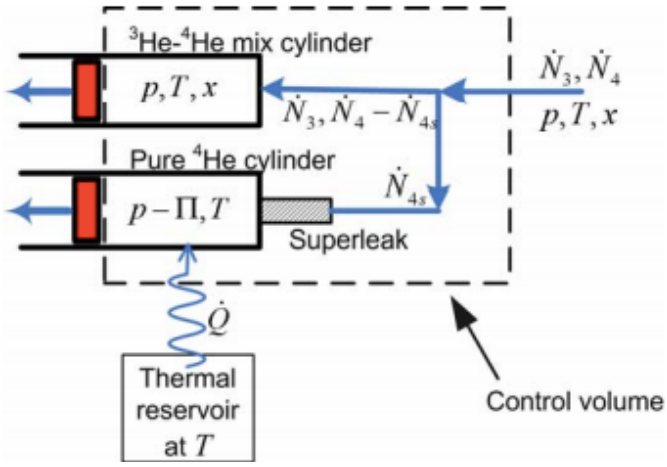

Figure 22. Gedanken experiment used to derive osmotic enthalpy for ^{3}He-^{4}He mixtures [25].

top canister, this means that the enthalpy flow rate out is $(\dot{N}_3 + \dot{N}_4 - \dot{N}_{4s})h(p,T,x)$, where $h(p,T,x)$ is well defined enthalpy for bulk flow. The enthalpy flow out of the bottom canister is $\dot{N}_{4s}h_4^0(p-\Pi,T)$, where h_4^0 is the enthalpy for pure ^{4}He. Therefore, the First Law energy balance at steady state becomes:

$$0 = \dot{Q} + \dot{N}h_{flow} - \left(\dot{N}_3 + \dot{N}_4 - \dot{N}_{4s}\right)h(p,T,x) - \dot{N}_{4s}h_4^0(p-\Pi,T), \tag{11}$$

where $\dot{Q}$ is the rate of heat into the bottom canister and can be calculated using the Second Law balance on the bottom container [30]:

$$0 = \frac{\dot{Q}}{T} - \dot{N}_{4s}s_4^0(p-\Pi,T). \tag{12}$$

$\dot{Q}$ can then be solved for and substituted into Eq. 11. Gibbs free energy relationships, $g = h - Ts$ and $g = \mu_4 + x\left(\frac{\partial g}{\partial x}\right)_{T,p}$, and the equality between chemical potentials defined by Eq. 7 can then be used to simplify Eq. 11, giving:

$$\dot{N}h_{flow} = \left(\dot{N}_3 + \dot{N}_4 - \dot{N}_{4s}\right)h(p,T,x) + \dot{N}_{4s}\mu_4(p,T,x). \tag{13}$$

We also know that the concentration in the top canister is simply $\dot{N}_3/(\dot{N}_3 + \dot{N}_4 - \dot{N}_{4s})$, which means:

$$\dot{N}h_{flow} = \frac{\dot{N}_3}{x}\,h(p,T,x) + (\dot{N}_3 + \dot{N}_4 - \frac{\dot{N}_3}{x})\mu_4(p,T,x) \tag{14}$$

This can be rearranged to find the final definition of both osmotic enthalpy given in Eq. 9, and the two terms that comprise the total flow enthalpy given in Eq. 10:

$$\dot{N}h_{flow} = \dot{N}_3\left(\frac{h(p,T,x)}{x} + \frac{(x-1)}{x}\mu_4(p,T,x)\right) + \dot{N}_4\mu_4(p,T,x)$$
$$= \dot{N}_3 h^{os}(p,T,x) + \dot{N}_4\mu_4(p,T,x). \quad (15)$$

For modeling the AMRR system, this representation of enthalpy is crucial for capturing the behavior of both the bulk fluid and the superfluid. The bulk flow enthalpy, *h*, as well as other thermodynamic properties for a ^{3}He-^{4}He mixture, such as the specific volume, *v*, heat capacity, *c*, and concentration, *x*, are taken from Chaudhry, who fit property curves to smoothed data sets for ^{3}He-^{4}He mixtures [25]. Because there is a lack of consistent data in the region of interest, it should be acknowledged that there are limitations to the accuracy of these fits.

3 Design of AMRR System

3.1 Introduction

The development of a proof-of-concept AMRR system relies on the proper design of each component to ensure that there is enough paramagnetic material and sufficient magnetic field to force circulation of the fluid and manipulate the temperature of the ^{3}He-^{4}He mixture throughout the system. The objective of the proof-of-concept AMRR is to provide measurable cooling at the CHX with this novel cycle. Simulating the behavior of the system with a high level of accuracy is difficult because of the large number components that interact throughout the multi-process cycle. These components do not only interact at their boundaries but also by redistribution of the different components of the mixture in order to satisfy both continuity and equilibration of chemical potential. In particular, there is nearly instantaneous movement of superfluid in the system that is driven to maintain uniform chemical potential. The simulation is further complicated by the complex dependence of the helium properties and the magnetocaloric material properties on multiple state variables, leading to a highly nonlinear system. For the development of a proof-of-concept system, a simplified model of the AMRR focusing on a single regenerator is adequate to inform the design process as it allows the approximate determination of the required cooling capacity of the regenerator without attempting to entirely capture the complexities of the AMRR system. As a functional SMP already exists in the UW-Madison SEL, this process primarily focused on the design of the remaining components that are required to complete the AMRR system: the superconducting regenerator magnets, regenerator canisters, and CHX.

3.2 AMRR Cycle Design Model

In order to properly design the remaining AMRR components so that they match the existing SMP, a model is required to guarantee refrigeration at the desired temperature. A simple model was developed focusing on a single AMRR regenerator, and the subsequent magnet and CHX models were developed based on the results of this model. For a more complete understanding of these models, an introduction to and explanation of the AMRR cycle processes is necessary.

3.2.1 AMRR Cycle Description

The AMRR cycle consists of four main processes which repeat in the following order: No Flow Demagnetization (NFD), Flow Demagnetization (FD), No Flow Magnetization (NFM), and Flow Magnetization (FM). Each side of the system is identical in construction and they operate 180° out of phase from each other. This means that while one side is in the NFD or FD process, the opposite side is in the NFM or FM process, respectively. Because of this tandem operation, it is important to understand that the explanation of each process is representative of the behavior of just one side of the AMRR, which consists of one regenerator, one SMP canister, one hot heat exchanger (HHX), and half of the CHX. A diagram of half of the system is shown in Figure 23.

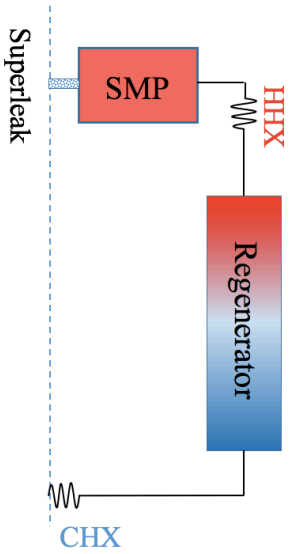

Figure 23. The RHS of the AMRR system.

The NFD process is shown in Figure 24, and begins with the regenerator at its maximum cycle magnetic field and temperature, and the SMP canister at its minimum cycle magnetic field and temperature. Field strength is represented by the blue ovals, with more lines indicating higher fields. The temperature is qualitatively represented by the color, with 1.7 K shown in dark red and 0.75 K shown in dark blue. During the NFD process, the SMP field is held constant, so there is no temperature change in the canister and no induced flow in the system. The regenerator is demagnetized, increasing the magnetic entropy of the GGG and lowering the temperature profile in the canister until the cold end temperature equals the inlet temperature of the CHX, designed to be at 0.75 K. At this point, the FD process can begin.

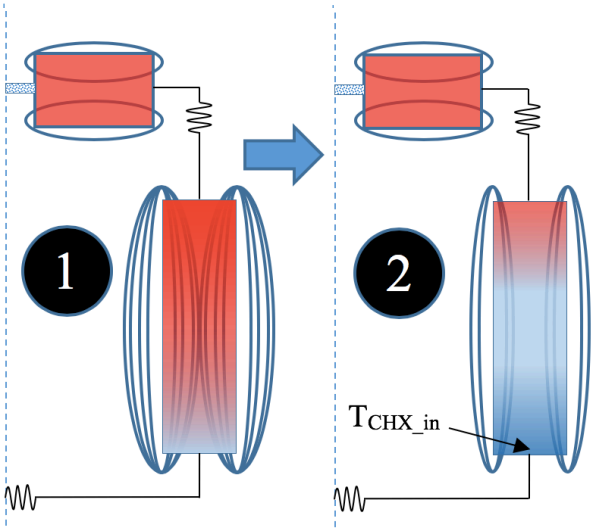

Figure 24. The start and end of the NFD process in the RHS of the AMRR.

During the FD process shown in Figure 25, the SMP canister is magnetized, warming the fluid and forcing the mixture into the rest of the system due to the previously explained fountain effect. Superfluid ^{4}He crosses the boundary into the warming canister during this process, driven to maintain a constant system chemical potential. The exiting mixture flows through the HHX into the

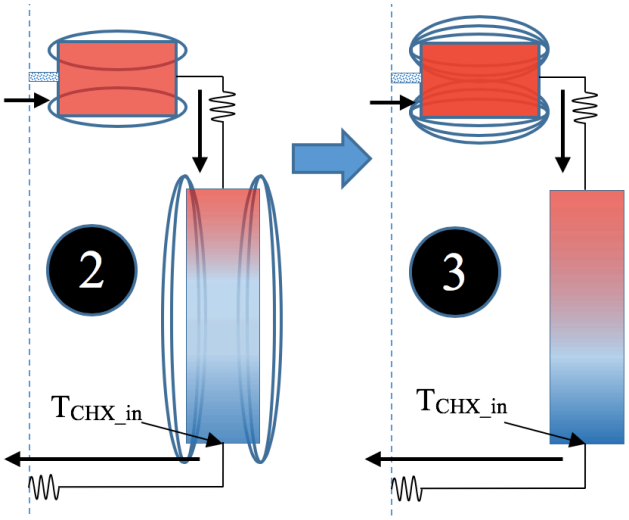

Figure 25. The start and end of the FD process in the RHS of the AMRR.

regenerator, which is still demagnetizing and cooling the fluid so that it exits at the desired CHX inlet temperature. The fluid then moves into the CHX, where a thermally linked instrument can reject heat into the mixture. The mixture exits the CHX into the opposite side of the AMRR. Eventually, the regenerator field depletes to 0 T, at which point the NFM process begins.

During the NFM process shown in Figure 26, the SMP canister has a constant field and temperature, resulting in no flow in the system. This is similar to the NFD process, except the SMP canister is now at its maximum temperature and field. The regenerator magnetizes at a constant rate, warming the temperature of the entrained fluid. This magnetization continues until the opposite side of the AMRR, in the NFD process, has a low end regenerator temperature equal to the desired CHX inlet temperature. At this point, flow can begin again in the opposite direction, and the system moves into the final process: FM.

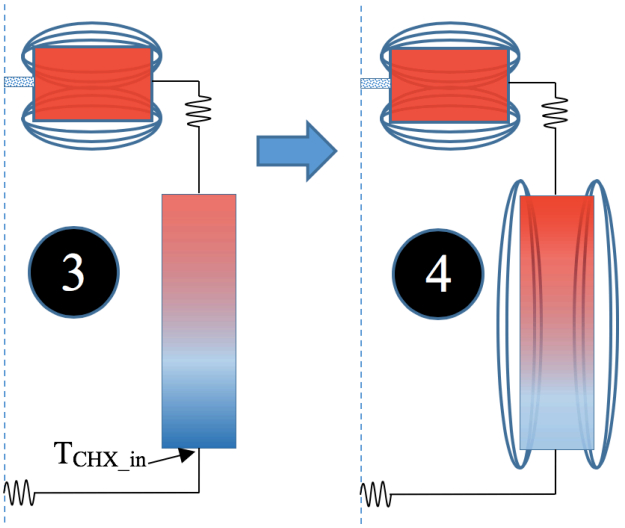

Figure 26. The start and end states of the NFM process in the RHS of the AMRR.

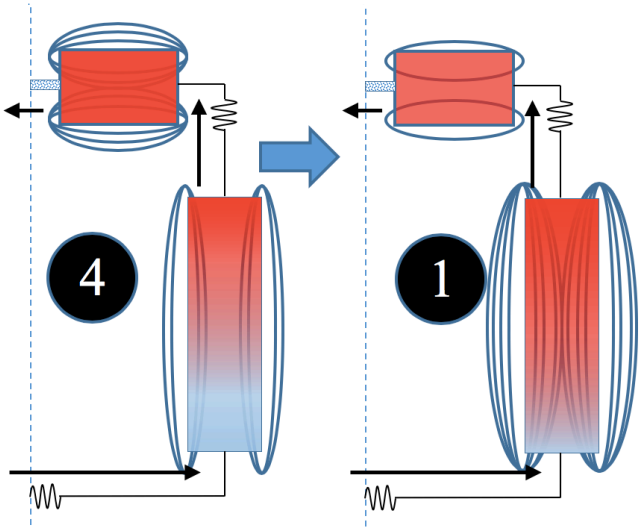

Figure 27. The start and end states of the FM process in the RHS of the AMRR.

In the final system process, shown in Figure 27, the SMP canister demagnetizes, lowering the temperature

and drawing in fluid from the system as superfluid ^{4}He exits through the superleak into the warming canister. The regenerator continues to magnetize, warming the incoming fluid from the CHX. After moving through the regenerator, the mixture rejects heat at the HHX and enters the cooling SMP canister. This process continues until the maximum magnetic field is reached in the regenerator and the minimum field is reached in the SMP canister. The completion of this process returns the AMRR system to its initial state and thus represents the completion of a single cycle.

3.2.2 Simple Design Model for AMRR

As previously noted, the simple design model focuses on one AMRR regenerator. The model conservatively assumes a constant linear temperature profile in the regenerator during the flow processes, and uses values that are consistent with a simple pump model for total moles of mixture flowing into and out of each regenerator at the respective HHX and CHX temperatures. The pump model uses the actual SMP canister volumes and assumes a specified temperature swing during the flow process. The corresponding concentration swing can be used to determine the total moles of mixture forced into the system during the process. Given a regenerator canister internal diameter (ID) and assumed field swing, a total process energy balance on the regenerator can be performed to determine the necessary length of the canister, ensuring that enough GGG is present to cool the entrained and entering fluid to achieve the desired outlet temperature.

The control volume (CV) for the regenerator is shown in Figure 28, where fluid enters from the HHX on the left and exits to the CHX on the right. It should be noted that the CV contains only what is within the black dashed line, i.e. the fluid mixture, and excludes the GGG

particles, which are represented by the solid black box. The magnetocaloric effect is captured through the heat exchange between the fluid and particles at the CV boundary.

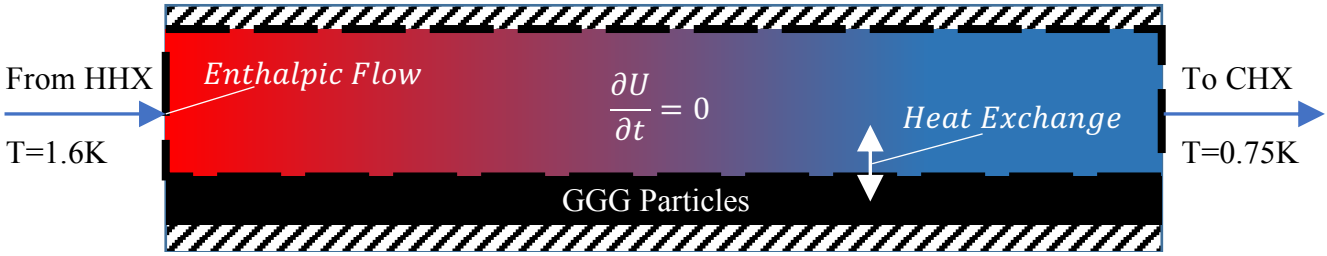

Figure 26. Control volume for regenerator canister. Fluid enters from the HHX at the left and exits to the CHX on the right.

The enthalpic flow into and out of the regenerator, heat exchange between the GGG particles, and internal energy of the fluid comprise the first law energy balance. As derived in Section 2.3.3, the enthalpic flow of a ^{3}He-^{4}He mixture is captured through:

$$\dot{N}h_{flow} = \dot{N}_3 h^{os}(p,T,x) + \dot{N}_4 \mu_4(p,T,x), \tag{15}$$

which, for the regenerator, becomes:

$$Nh_{flow} = N_3 h_{in}^{os}(T_{HHX}, x_{HHX}) + N_{4,in}\mu_4(T_{HHX}, x_{HHX}) - N_3 h_{out}^{os}(T_{CHX}, x_{CHX}) - N_{4,out}\mu_4(T_{CHX}, x_{CHX}) \tag{16}$$

where the enthalpy is evaluated at the HHX and CHX temperatures and concentrations. N_3 is the number of moles of ^{3}He that exit the pump, and is assumed to be the total number of moles of ^{3}He both into and out of the regenerator because it is viscously interlocked with the bulk fluid. N_4, on the other hand, is the adjusted number of moles of ^{4}He, corrected using the concentrations at the entrance and exit to capture the change due to superfluid motion.

In order to calculate the heat exchange between the fluid and GGG, the total entropy change in the GGG is multiplied by the temperature. To increase the accuracy of this calculation, the regenerator is divided into spatial (i=1...N) and temporal (j=1...M) nodes to

effectively integrate the total heat from the GGG during the process. The energy from the GGG is obtained using the equation below summed over all spatial and temporal nodes:

$$Q_{GGG,i,j} = T_{i,j} \cdot n_{GGG} \left(\left. \frac{\partial s}{\partial T} \right|_{T=T_{i,j}} \left(T_{i,j+1} - T_{i,j}\right) + \left. \frac{\partial s}{\partial B} \right|_{B=B_j} \left(B_{j+1} - B_j\right) \right), \tag{17}$$

where $Q_{GGG,i,j}$ is the heat from the GGG into the fluid in node i at timestep j, n_{GGG} is the number of moles of GGG associated with the node, and the partial derivatives of the entropy are multiplied by the respective changes in temperature and field over a timestep. For the constant linear temperature profile that is assumed in the simple model, this equation can be simplified to:

$$Q_{GGG,i,j} = T_i \cdot n_{GGG} \left(\left. \frac{\partial s}{\partial B} \right|_{B=B_j} \left(B_{j+1} - B_j\right) \right). \tag{18}$$

The field changes at a constant rate between the maximum beginning field and ending field of 0 T, so B_j is simply:

$$B_j = B_{max} - (j-1) \cdot \frac{B_{max} - 0}{M - 1}. \tag{19}$$

Finally, the internal energy of the regenerator is assumed to not change during the process as the temperature profile is constant. Though this is not entirely representative of what will actually occur during a cycle, the approach overestimates the required cooling capacity of the regenerator and is therefore a reasonable approach for design. Combining Eqs. 15 and 19 gives a first law energy balance of node i:

$$0 = \sum_{j=1}^{M} \sum_{i=1}^{N} Q_{GGG,i,j} + N h_{flow} \tag{20}$$

From this equation, it is possible to determine the required length of the regenerator for a given canister ID based on the number of moles of GGG required per node.

Following the determination of the final regenerator sizing using this simple model, a code to design the corresponding regenerator magnets was created. The dimensions of the canister and required field swing were used to constrain the magnet design. The equation for the magnetic field along the axis of a solenoid is derived in Jahromi's PhD thesis, defended at the University of Wisconsin-Madison in 2015, and is given as:

$$B_{axis,inside} = \frac{\mu_0 nI}{2}\left[\frac{x_2}{\sqrt{x_2^2 + R_{coil}^2}} + \frac{L_{coil} - x_2}{\sqrt{(L_{coil} - x_2)^2 + R_{coil}^2}}\right], \quad (21)$$

where μ_0 is the permeability of free space, $4\pi \times 10^{-7}$ (N/A^2), n is the total turns per unit length, I is the current in the coil, x_2 is the axial location, L_{coil} is the length of the coil, and R_{coil} is the effective radius of the coil, calculated at half of the coil thickness [9]. This equation can be used to find the required total number of turns for a given mandrel geometry to reach the desired field at the center of the coil. For the regenerator, the magnets were designed to reach a maximum of 1.5 T, more than twice the required field for FD process according to the simple model.

3.3 Final AMRR Component Designs

Using both the simplified regenerator model and magnet design code, the remaining AMRR components were finalized in SolidWorks. It should be noted that due to an unforeseen limitation on the available traverse length of coil winder, the initial design length of the coil exceeded the possible wind length of the machine by 1.7 cm. To adjust for this, a collar was fit to the magnet mandrel at the maximum winding length, and crushed glass was used to

replace a small portion of the GGG. The final design still exceeded the required regenerator length and field strength calculated by the simple design code.

3.3.1 Final Regenerator Design

The final regenerator design includes the canister pieces, magnet mandrel and winding specifications, and suspension system for thermally isolating and centering the canister within the bore of the magnet. The final design, with the adjustment collar and glass, is shown in Figure 29.

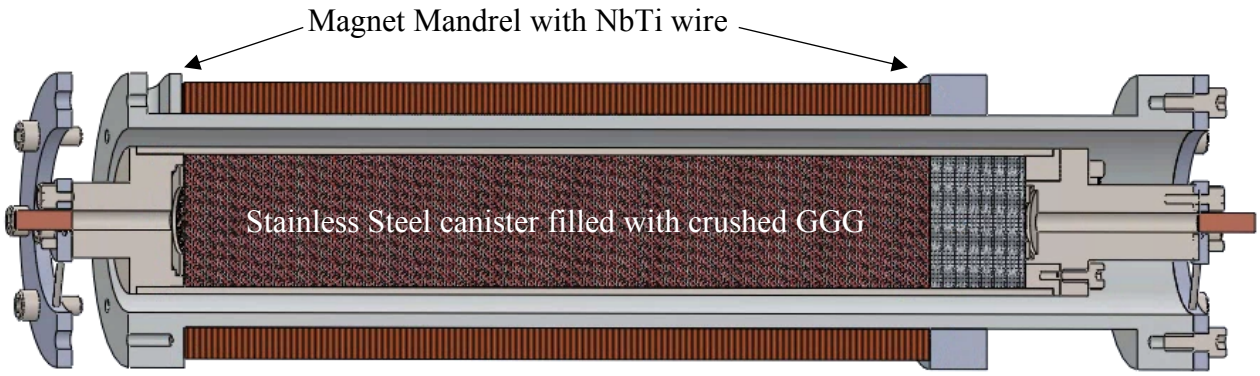

Figure 27. Cross-sectional view of the final regenerator design, which includes the canister, suspension, and magnet.

The regenerator canister is composed of four stainless steel pieces: the thin-walled tube and three end caps. Two of these end caps are welded to the tube, one with an opening to allow for packing, and the third is sealed into the open cap with indium after the canister is packed with GGG. Inlet and outlet headers are included in the endcaps to allow for even flow distribution radially within the regenerator. Fine mesh screens are used to prevent the movement of GGG particles into these volumes, consequently preventing the displacement of GGG into the remainder of the system. Because GGG has a relatively large heat capacity under these conditions (which would be undesirable in the unmagnetized portion of the bed), crushed

glass with the same particle size and fill porosity as the GGG was used to fill the extra volume beyond the magnet length as its heat capacity approaches zero at the temperatures within the regenerator.

The regenerator magnet consists of a niobium-titanium (NbTi) coil potted in an aluminum mandrel. The wire chosen contains 54 NbTi filaments, each with a diameter of 9 μm, embedded in a stabilizing copper matrix with a total insulated diameter of 0.127 mm. This diameter, along with a conservative current of 4.7 A, was used to determine the number of turns required to reach 1.5 T in the center of a magnet. The magnetic field at the center of the regenerator as a function of axial location is shown in Figure 30. Though there are significant

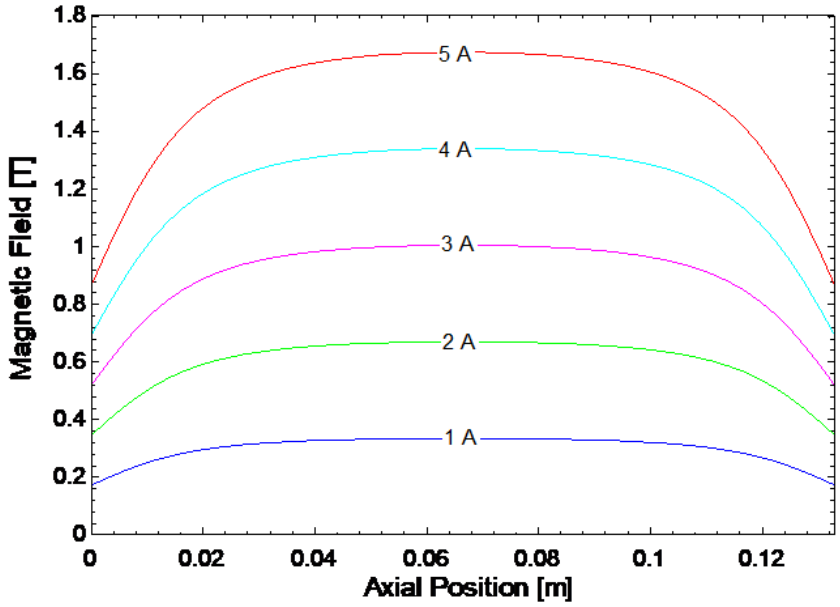

Figure 28. Magnetic field at center axis as a function of axial location for different currents.

edge effects, the magnet is strong enough to provide the required cooling within the regenerator. A few additional considerations in the mandrel design were necessary to ensure safe operation of the magnet. For example, the mandrel wall must be thick enough to withstand the hoop stress of the coil and additional forces when the coil is magnetized. Additionally, the

mandrel must be thick enough to effectively reject heat from the coil in the event of a quench. A diode pocket in one of the flanges of the magnet is necessary to prevent damaging the coil if a quench does occur. When this happens, the coil transitions into a normal state and the voltage across the coil leads increases above the forward voltage of the diodes, effectively rerouting the current through the diodes to dissipate heat in the coil.

The final regenerator component, the suspension, is composed of a center disk suspended by Kevlar within a thin aluminum ring. This suspension is shown in Figure 31 and is identical on both sides of the regenerator. The center disk attaches to the regenerator canister, while the outer ring is supported by the magnet mandrel, centering the canister within the bore of the magnet. Kevlar is incredibly strong in tension, having a tensile strength around 2.5 GPa, and also has a very low thermal conductivity. These qualities make it an attractive option for use in suspending and thermally isolating the canister.

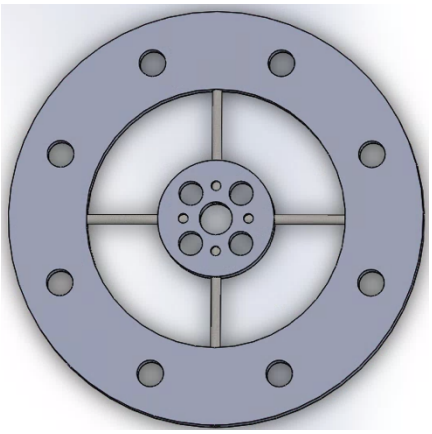

Figure 29. The suspension design for centering the canister within the bore of the magnet.

A summary of key final regenerator design parameters is provided in Table 5:

Table 5. A summary of key final regenerator canister and magnet parameters.

Regenerator Canister		Regenerator Magnet	
Canister Material	304 Stainless Steel	Mandrel Material	6061 Aluminum
ID [m]	0.0229 m	ID [m]	0.03175 m
OD [m]	0.0254 m	OD [m]	0.0508 m
Porosity [-]	0.38	Coil Material	54S43 NbTi
GGG Fill Length [m]	0.133 m	Coil Length [m]	0.133 m
Glass Fill Length [m]	0.017m	Current [A]	4.7 A
Total Mass GGG [kg]	0.240 kg	Number of Turns [-]	37,000
Total Mass Canister [kg]	0.204 kg	Max Field [T]	1.5 T

3.3.2 Final CHX Design

The final component required to complete the AMRR system is the CHX. The design of this heat exchanger is relatively straightforward, and assumes a small approach ΔT and fully developed laminar flow in the pipe. Additionally, the tube surface is assumed to be at a constant temperature equal to the detector temperature. The inlet and outlet temperatures are 0.75 K and 0.90 K, respectively, and are used to determine the total rate of heat transferred into the fluid in the cold heat exchanger, which is estimated to be around 1 mW. The minimum length for a ΔT equal to 0.02 K is 22.4 cm, putting a lower bound on the length of the CHX. Design and construction of the HHXs was included the original SMP assembly, so the completion of the regenerator and CHX designs represents the conclusion of the AMRR system design phase.

4 Construction and Assembly of AMRR System

4.1 Introduction

Following the finalization of their designs, construction of the remaining AMRR components began. This included machining the canister, mandrel, and suspension components, winding the magnets, and crushing and packing the GGG into the canister. Additionally, brackets for suspending the regenerators within the Dewar were machined. These components will be assembled together to complete the AMRR system.

4.2 Canister Assembly

4.2.1 Machined Components

As previously mentioned, the canister assembly consists of one thin-walled tube and three endcaps, all machined out of stainless steel. A sample of two of the endcaps is shown in Figure 32. The endcap on the left is welded to the end of the tube to provide a sealing surface once the GGG has been packed, and has a large through hole to allow for packing and for a header volume to better distribute incoming fluid. The endcap on the right screws into the one on the left, pulling down on the indium ring between the two pieces to prevent leaks. Two mesh screens are fit into the header volume to prevent GGG particles from circulating with the fluid. The third endcap is similar to the one on the right, in that it has a header volume blocked by screens, but it does not have through holes as it is welded onto the opposite side of the canister. One complete regenerator is shown in Figure 33 below. Brazed

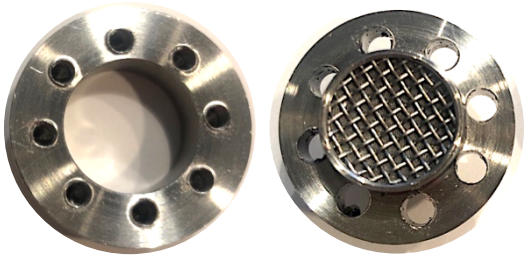

Figure 30. An example of two of the three canister endcaps.

into each outermost endcap is a short length of copper tubing to allow for easy integration with the rest of the system.

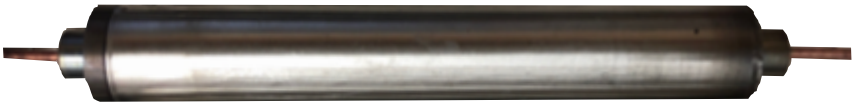

Figure 31. One complete regenerator canister.

4.2.2 GGG Crushing and Packing Method

Though GGG crushes into irregular shapes, the target particle size was roughly ≤1 mm in diameter. To achieve this, two sieves with 1.2 mm and 0.2 mm hole widths were used to create a go no-go gage. Figure 34 shows an image of the sieves taken during the crushing

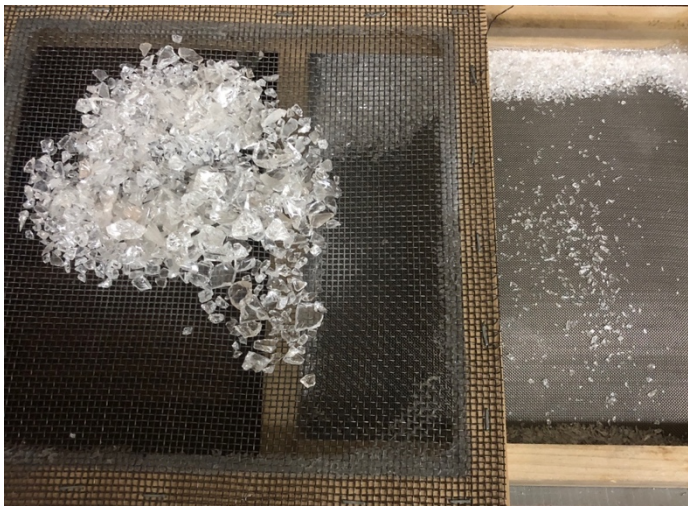

Figure 32. Sieves used in crushing process to ensure correct particle size.

process. Large chunks of the crystal were hammered into finer pieces, which were placed on top of the wider sieve and shaken to ensure that all particles with diameter <1.2 mm would pass through into the second sieve. The particles collected in the second sieve could be used to pack the canister beds. Any finer particles that passed through the second sieve were discarded. The glass used to replace a portion of the GGG was crushed following the same procedure.

In order to realize the optimal porosity of 0.38 in the canisters, the required mass of GGG to fill 62% of the internal GGG volume was determined. This mass was slowly packed into the canister, and the canister was shaken throughout to allow the particles to evenly distribute. Once filled, the canister end caps were screwed on and the canister was shaken to allow the particles to settle further. The canister was then reopened, and the small void from settling was filled. This process was repeated until there was no void from settling to guarantee the particles were packed tightly and would not shift during operation.

4.3 Magnet Construction

Thick walled 6061 Aluminum tubing was used to create the magnet mandrels. The outer radius was turned down using a lathe to create flanges on either side of the winding length and reach the required mandrel thickness. On one flange, the diode pocket and inlet channel were machined to allow for the entry and exit of the wire into the coil. An additional collar was designed to modify the magnet length based on the allowable traverse of the winder. The collar was clamped onto the winding surface of the mandrel using epoxy to create a smooth and continuous surface. Following the machining of the magnet mandrels and collar, the mandrel was prepared for winding.

The winding surface and flanges were polished using 6 different 3M polishing papers, which stepped down from 30 micron paper to 1 micron paper. Polishing the mandrel is crucial because even small imperfections on the surface could cut through the wire insulation under the immense force of the winding and short the coil to the mandrel. Once polished, the surface was extensively cleaned to remove any paper fibers or residue from machining. Then, 0.025 mm thick Kapton tape was used to wrap the winding surface and flanges. This further protects

against shorts by effectively creating a backup insulation layer between the coil and mandrel. The Kapton layer also minimally increases the thermal resistance between the coil and mandrel, which is an important consideration in the event of a quench when the coil must reject heat to the mandrel. The mandrel is then secured in the magnet winding machine.

Prior to winding, wire is wrapped around one of the flanges to provide an adequate lead length for installation into the Dewar once the magnet is wound. This wire is taped to the flange and then fed through the diode pocket into the mandrel and secured at the entry point. Care is taken to not wrap the wire tightly around one edge of the channel when entering the winding surface. A picture of this setup is shown in Figure 35.

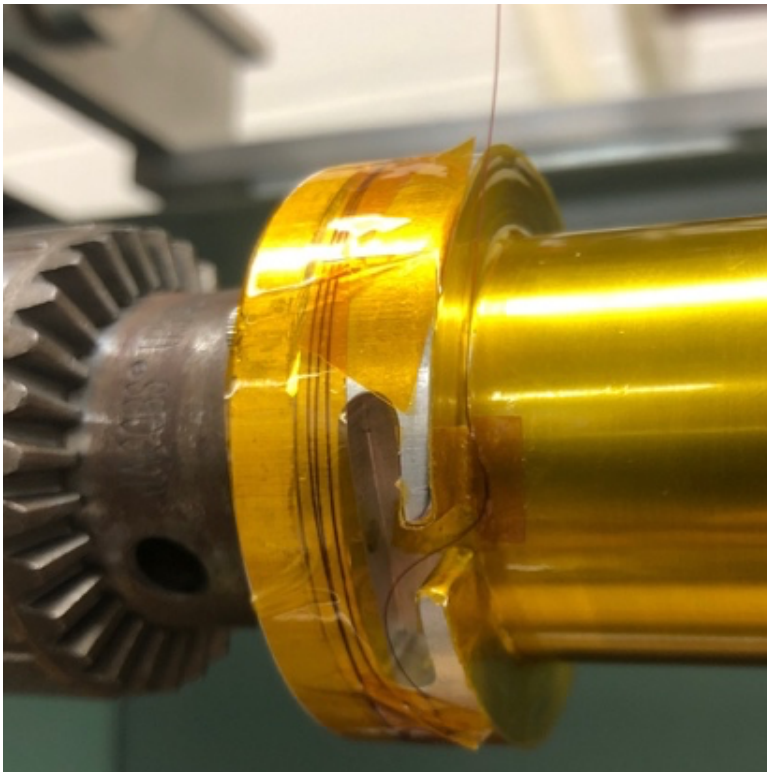

Figure 33. Complete magnet mandrel setup prior to winding.

One final step to prepare for winding was the preparation of the CTD-A521 magnet epoxy. A small batch was made and degassed to place on the mandrel to start, and then a new batch was made every hour as this was about how long it took for the epoxy to begin curing. The epoxy was continuously brushed onto the coil throughout the winding process using a silicone bristle brush. Potting the coil in epoxy helps prevent frictional heating in the magnet by preventing movement due to forces created during magnetization and

demagnetization. The epoxy also helps to create good thermal contact between the wires and mandrel.

Once the number of required turns was reached and the wire returned to the diode pocket side of the mandrel, the winding operation ended. Similarly to the process at the start of the magnet, the wire was fed into the diode pocket and a lead length was wrapped around the flange and taped down. The magnet was then slowly rotated on the winding machine for at least 24 hours as the epoxy cured in order to prevent the epoxy from running off or distorting the coil. An image of the magnets following the winding process is shown in Figure 36.

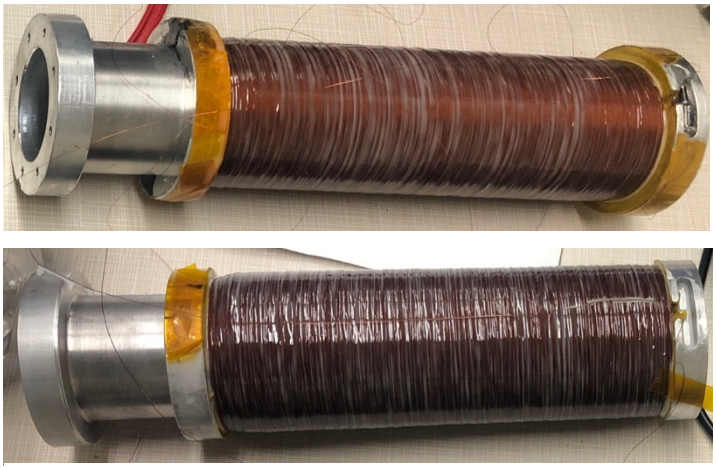

Figure 34. The magnets following winding.

To finish the magnets, the wire insulation in the diode pockets was stripped, and then soldered to the ends of two 1N4001 diodes that were placed in opposite directions in the pocket. As noted previously, the current is redirected through these diodes in the event of a quench, when the voltage across the coil leads exceeds the forward voltage of the diodes. They are placed back to back so that the direction of the applied current does not matter. The diode pockets were then filled with the CTD-A521 epoxy, signifying the completion of the magnets.

4.5 Entire AMRR Assembly

Prior to installing the AMRR system into the Dewar, suspension components had to be machined. These included copper end brackets for the magnets and suspension rings for

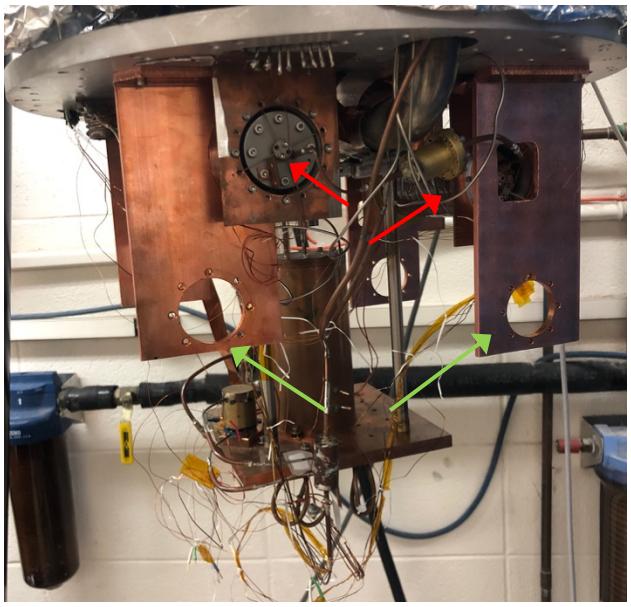

Figure 35. Partial AMRR assembly in Dewar.

centering the canisters within the mandrels. The copper brackets have the same conduction resistance from the magnet to the 4 K plate as the preexisting copper brackets used with the SMP canisters, ensuring that the magnet will not heat up too much in the event of a quench. The brackets have been positioned within the Dewar to suspend the regenerator canisters parallel and approximately below pump canisters, as shown in Figure 37. The red arrows indicate the locations of the two SMP canisters, and the green arrows point towards the regenerator support brackets. The circulation path will be configured so that while one regenerator is magnetizing, the above pump canister is also magnetizing and vice versa so as to minimize deconstructive interference with the magnetic fields.

The HHXs that will be used in the AMRR system are already integrated into the Dewar, and are attached to the bottom of the 1 K stage. The temperature of this platform can be controlled by a heater to maintain a precooling temperature around 1.6 K. The CHX consists of tubing attached to a copper plate with a contact length that matches the design length. The CHX plate also has a heater attached to allow control and measurement of the cooling power of the system. This heat exchanger will be suspended from the bottom of the 1 K plate to thermally isolate it and minimize parasitic loads.

Finally, one of the SMP magnets had failed prior to SMP testing and needed to be replaced with a new magnet, which had been designed to provide the same inductance as the

existing magnet. A cooldown to test this replacement magnet went well, with a quench only occurring above 5 A, well above the current required to run the SMP. However, this test also showed unreliable behavior of the other SMP magnet, which was previously assumed to be operational. To have control over the system without concerns of failure during testing, this magnet also needs to be replaced. A new magnet with the same dimensions and field strength was designed to be installed in the failed magnet's place. Once the new magnet is complete, the entire AMRR system can be assembled in the Dewar and experimental testing can begin.

6 Conclusions and Future Work

This work focused on the design and development of a complete proof-of-concept AMRR system using GGG as the refrigerant with a ^{3}He-^{4}He working fluid. Though the utilization of the magnetocaloric effect for low temperature refrigeration is not novel, the combination of this technique and the exploitation of exceptional near Kelvin Helium properties to provide distributed sub-Kelvin cooling with no moving parts is truly unique. Once optimized, this system can be used to provide precooling to lower temperature stages or for distributed cooling over large areas offering an improvement over current systems and making new types of cryogenic refrigeration configurations possible.

The SMP used to create circulation within the AMRR system has already been developed and tested at UW-Madison. The remaining components, i.e. the heat exchangers and regenerators, were designed to be consistent with this existing pump and provide measurable cooling at the cold end. The two regenerator magnets were designed to reach fields of 1.5 T, more than twice the predicted required field determined using the simple thermodynamic system model to account for system unknowns and modeling assumptions. Each regenerator canister was filled with GGG particles approximately 1mm or less in diameter to a design porosity of 0.38, and then sealed through welding, brazing, and indium rings. The regenerator canisters were then suspended within the magnets to complete the regenerator construction.

During a cooldown, a preexisting SMP magnet presumed to be functional was found to not be operating reliably. A new magnet has been designed to replace this one and, once constructed, the entire AMRR system can be assembled as the remaining components are complete.

Near future work includes finishing the assembly of the AMRR system, testing the functionality of the new magnets, and experimentally validating the system. This will require the development of a LabView program to establish control over the four independent magnets and system heaters, including a feedback loop to demagnetize the regenerator at a variable rate that ensures a constant outlet temperature. Prior to running the system, it must be leak checked. Additionally, it may be valuable to run the SMP with both canisters prior to running the entire system as previous testing only used one side of the pump.

Once the AMRR developed in this work has been experimentally tested, the author intends to redesign the system using GLF as the paramagnetic regenerator refrigerant, which will allow the system to reach temperatures as low as 0.35 K, substantially lowering the cold end temperature. The insights gained from the GGG design will allow for a more optimal design and a more thorough understanding of the operating space of the system.

Finally, the development of a comprehensive AMRR numerical model would be useful in future system design and optimization, especially for advancing the system technology towards providing reliable cooling for space-flight applications. The data from the GGG and GLF AMRR systems can be used to experimentally validate this model.

References

[1] P. Shirron, *Chloe Gunderson NSTRF Progress Report,* [Email]. 2018.

[2] N. Rando, D. Lumb, M. Bavdaz, D. Martin and T. Peacock, "Space science applications of cryogenic detectors," in *Advanced Transition Radiation Detectors for accelerator and space applications*, Bari, Italy, 2003.

[3] N. Rando, "Cryogenics in Space," in *Observing Photons in Space*, New York, NY, Springer, 2013, pp. ISSI Scientific Report Series, vol 9.

[4] Figueroa Group, "The Ideal Microcalorimeter," Experimental Cosmology and Astrophysics Laboratory, MIT, 2014. [Online]. Available: http://web.mit.edu/figueroagroup/ucal/ucal_basics/index.html. [Accessed 20 3 2020].

[5] D. McCammon, "Thermal Equilibrium Calorimeters -- An introduction," in *Cryogenic Particle Detection*, vol. 99, Berlin, Springer, 2005.

[6] L. Duband, J. Duval, N. Luchier and T. Prouve, "SPICA sub-Kelvin cryogenic chains," *Cryogenics,* vol. 52, pp. 145-151, 2012.

[7] NASA, "2020 NASA Technology Taxonomy," 2020. [Online]. Available: https://www.nasa.gov/sites/default/files/atoms/files/2020_nasa_technology_taxonomy.pdf. [Accessed 20 March 2020].

[8] P. Shirron, D. Wegel, M. DiPirro and S. Sheldon, "An adiabatic demagnetization refrigerator for continuous cooling at 10 mK and below," in *AIP Conference*, 2006.

[9] A. E. Jahromi, "Development of a Proof of Concept Low Temperature Superfluid Magnetic Pump with Applications," PhD dissertation at University of Wisconsin-Madison, 2015.

[10] T. Tirolien, P. Camus, G. Vermeulen, A. Volpe, S. Triqueneauz, A. Benoit, J. Butterworth and S. d'Escrivan, "Status of the Closed-Cycle Dilution Refrigerator Development for Space Astrophysics," *Journal of Low Temperature Physics,* vol. 176, pp. 5-6, 2013.

[11] M. Sauvage, K. Okumura, U. Klaas, T. Muller, A. Moor, A. Poglitsch, H. Feuchtgruber and L. Duband, "Operations and performance of the PACS instrument ^{3}He sorption cooler on board of the Herschel space observatory," *Exp Astron,* vol. 37, pp. 397-431, 2014.

[12] L. Duband, L. Clerc, E. Ercolani, L. Guillemet and R. Vallcorba, "Herschel flight models sorption coolers," *Cryogenics,* vol. 48, pp. 95-105, 2008.

[13] C. Day, "Basics and Applications of Cryopumps," *CAS - CERN Accelerator School : Vacuum in Accelerators,* pp. 241-274, 2007.

[14] V. K. Pecharsky and K. A. Gschneider Jr., "Magnetocaloric effect and magnetic refrigeration," *Journal of Magnetism and Magnetic Materials,* vol. 200, pp. 44-56, 1999.

[15] P. Wikus, E. Canavan, S. T. Heine, K. Matsumoto and T. Numazawa, "Magnetocaloric Materials and the Optimization of Cooling Power Density," *Cryogenics,* 2014.

[16] P. J. Shirron, "Applications of the Magnetocaloric Effect in Single-Stage, Multi-Stage and Continuous Adiabatic Demagnetization Refrigerators".

[17] P. Schiffer, A. P. Ramirez, D. A. Huse and A. Valentino, "Investigation of the Field Induced Antiferromagnetic Phase Transition in the Frustrated Magnet: Gadolinium Gallium Garnet," *Physical Review Letters,* vol. 73, no. 18, pp. 2500-2503, 1994.

[18] Cryogenics and Fluids Branch, "Introduction to Liquid Helium," NASA Goddard Space Flight Center, 11 9 2014. [Online]. Available: https://cryo.gsfc.nasa.gov/introduction/liquid_helium.html. [Accessed 13 8 2020].

[19] P. Wolfle and D. Vollhardt, The Superfluid Phases of Helium 3, Mineola, New York: Dover Publications, Inc., 1990.

[20] D. A. Shea and D. Morgan, "The Helium-3 Shortage: Supply, Demand, and Options for Congress," Congressional Research Service, 2010.

[21] A. Cho, "Helium-3 Shortage Could Put Freeze on Low-Temperature Research," *Science,* pp. 778-779, 2009.

[22] S. H. Harrison, M. W. Henley, K. Kuhlman, G. L. Kulcinski, J. F. Santarius and L. A. Taylor, "Lunar Helium-3 Fusion Resource Distribution," NASA Solar System Exploration, 2017.

[23] S. V. Sciver, Helium Cryogenics, New York, NY: Springer, 2012.

[24] D. Papoular, G. Ferrari, L. P. Pitaevskii and S. Stringari, "Increasing Quantum Degeneracy by Heating a Superfluid," *Physical Review Letters,* vol. 109, 2012.

[25] G. Chaudhry, "Thermodynamic properties of liquid ^{3}He-^{4}He mixtures between 0.15 K and 1.8 K," PhD dissertation at Massachusetts Institute of Technology, 2009.

[26] R. Radebaugh, "Thermodynamic properties of ^{3}He-^{4}He solutions with applications to the ^{3}He-^{4}He dilution refrigerator," NBS Tech note 362:19, 1967.

[27] R. de Bruyn Ouboter, K. W. Taconis, C. le Pair and J. M. Beenakker, "Thermodynamic properties of liquid ^{3}He-^{4}He mixtures derived from specific heat measurements between 0.4K and 2K over the complete concentration range," *Physica,* vol. 26, pp. 853-888, 1960.

[28] T. Alvesalo, P. Bergland, S. Islander, G. Pickett and W. Zimmermann Jr., "Specific Heat of Liquid ^{3}He/^{4}He Mictures near the Junction of teh lambda and Phase-Separation Curves. I," *Physical Review A,* vol. 4, pp. 2354-2368, 1971.

[29] H. London, G. Clarke and E. Mendoza, "Osmotic Pressure of ^{3}He in Liquid ^{4}He, with Proposals for a Refrigerator to Work below 1 K," *Physical Review,* vol. 128, pp. 1992-2005, 1962.

[30] F. Miller and J. Brisson, "A simple method for the analysis of sub-Kelvin refrigerators that use a dilute superfluid ^{3}He-^{4}He mixture as a working fluid," *Cryogenics,* vol. 41, pp. 311-318, 2001.

[31] C. Ebner and D. Edwards, "The low temperature thermodynamic properties of superfluid solutions of ^{3}He in ^{4}He," *Physics Reports,* vol. 2, pp. 77-154, 1971.

[32] Cryogenic Engineering Group, "Cryocoolers for space applications," University of Oxford, [Online]. Available: http://www2.eng.ox.ac.uk/cryogenics/research/cryocoolers-for-space-applications. [Accessed 20 March 2020].